Detection of the 2175 Å UV bump at $z > 7$: evidence for rapid dust evolution in a merging reionization-era galaxy

Katherine Ormerod [1]★ Joris Witstok [2,3] Renske Smit [1] Anna de Graaff [4] Jakob M. Helton [5]
Michael V. Maseda [6] Irene Shivaei [7] Andrew J. Bunker [8] Stefano Carniani [9]
Francesco D'Eugenio [10,11] Rachana Bhatawdekar [12] Jacopo Chevallard [8] Marijn Franx [13]
Nimisha Kumari [14] Roberto Maiolino [10,11,15] Pierluigi Rinaldi [5] Brant Robertson [16]
and Sandro Tacchella [10,11]

[1]*Astrophysics Research Institute, Liverpool John Moores University, 146 Brownlow Hill, Liverpool L3 5RF, UK*
[2]*Cosmic Dawn Center (DAWN), Copenhagen, Denmark*
[3]*Neils Bohr Institute, University of Copenhagen, Jagtvej 128, DK-2200 Copenhagen, Denmark*
[4]*Max-Planck-Institut für Astronomie, Königstuhl 17, D-69117 Heidelberg, Germany*
[5]*Steward Observatory, University of Arizona, 933 N. Cherry Avenue, Tucson, AZ 85721, USA*
[6]*Department of Astronomy, University of Wisconsin-Madison, 475 N. Charter St, Madison, WI 53706, USA*
[7]*Centro de Astrobiología (CAB), CSIC-INTA, Ctra. de Ajalvir km 4, Torrejón de Ardoz, E-28850 Madrid, Spain*
[8]*Department of Physics, University of Oxford, Denys Wilkinson Building, Keble Road, Oxford OX1 3RH, UK*
[9]*Scuola Normale Superiore, Piazza dei Cavalieri 7, I-56126 Pisa, Italy*
[10]*Kavli Institute for Cosmology, University of Cambridge, Madingley Road, Cambridge CB3 0HA, UK*
[11]*Cavendish Laboratory, University of Cambridge, 19 JJ Thomson Avenue, Cambridge CB3 0HE, UK*
[12]*European Space Agency (ESA), European Space Astronomy Centre (ESAC), Camino Bajo del Castillo s/n, E-28692 Villanueva de la Cañada, Madrid, Spain*
[13]*Leiden Observatory, Leiden University, NL-2300 RA Leiden, the Netherlands*
[14]*AURA for European Space Agency, Space Telescope Science Institute, 3700 San Martin Drive. Baltimore, MD 21210, USA*
[15]*Department of Physics and Astronomy, University College London, Gower Street, London WC1E 6BT, UK*
[16]*Department of Astronomy and Astrophysics, University of California, Santa Cruz, 1156 High Street, Santa Cruz, CA 96054, USA*

ABSTRACT

Dust is a fundamental component of the interstellar medium within galaxies, as dust grains are highly efficient absorbers of ultraviolet (UV) and optical photons. Accurately quantifying this obscuration is crucial for interpreting galaxy spectral energy distributions (SEDs). The extinction curves in the Milky Way (MW) and Large Magellanic Cloud exhibit a strong feature known as the 2175 Å UV bump, most often attributed to small carbonaceous dust grains. This feature was recently detected in faint galaxies out to $z = 7.55$, suggesting rapid formation channels. Here, we report the detection of a strong UV bump in a luminous Lyman-break galaxy at $z_{\rm prism} = 7.11235$, GNWY-7379420231, through observations taken as part of the NIRSpec Wide GTO survey. We fit a dust attenuation curve that is consistent with the MW extinction curve within 1σ, in a galaxy just ~ 700 Myr after the big bang. From the integrated spectrum, we infer a young mass-weighted age ($t_\star \sim 22$–59 Myr) for this galaxy, however spatially resolved SED fitting unveils the presence of an older stellar population ($t_\star \sim 252$ Myr). Furthermore, morphological analysis provides evidence for a potential merger. The underlying older stellar population suggests the merging system could be pre-enriched, with the dust illuminated by a merger-induced starburst. Moreover, turbulence driven by stellar feedback in this bursty region may be driving polycyclic aromatic hydrocarbon formation through top-down shattering. The presence of a UV bump in GNWY-7379420231 solidifies growing evidence for the rapid evolution of dust properties within the first billion years of cosmic time.

Key words: methods: observational – dust, extinction – galaxies: high-redshift – dark ages, reionization, first stars.

1 INTRODUCTION

Dust is a fundamental component of the interstellar medium (ISM) within galaxies, and affects the observed spectral energy distribution (SED) of galaxies over a broad wavelength range. Dust grains absorb approximately half of the optical and ultraviolet (UV) light and re-emit the absorbed energy as infrared light, which has important implications on the observational properties of galaxies (Kennicutt & Evans 2012; Schneider & Maiolino 2024). The dust attenuation curve of a galaxy describes how the integrated luminosity of a galaxy is affected by absorption and scattering of photons along

★ E-mail: arikorme@ljmu.ac.uk

the line of sight (LOS) due to dust in the ISM, and results from a combination of dust grain properties, dust content, and the spatial distribution of dust (e.g. Calzetti 2013; Salim & Narayanan 2020; Markov et al. 2023, 2025). An understanding of a galaxy's attenuation curve is crucial for the derivation of robust physical parameters, which can vary significantly depending on the assumed attenuation curve (e.g. Kriek & Conroy 2013; Reddy et al. 2015; Salim et al. 2016; Salim & Narayanan 2020; Shivaei et al. 2020; Markov et al. 2023).

Dust in galaxies can be characterized using both extinction curves, measured along sightlines to individual stars, and attenuation curves describing the integrated light of galaxies. Attenuation curves incorporate effects arising from the star–dust geometry within galaxies, such as scattering back into the LOS, and contribution from unobscured stars (Narayanan et al. 2018; Salim & Narayanan 2020). Common examples include the Calzetti attenuation curve (Calzetti, Kinney & Storchi-Bergmann 1994; Calzetti et al. 2000) derived for local starburst galaxies, and the Milky Way (MW) (Cardelli, Clayton & Mathis 1989), Small Magellanic Cloud (SMC), and the Large Magellanic Cloud (LMC) extinction curves (Fitzpatrick & Massa 1986; Gordon et al. 2003, 2024). The MW extinction curve exhibits a 'UV bump' feature at 2175 Å, while the LMC extinction curve contains a weaker UV bump, but stronger far ultraviolet (FUV) rise than the MW curve. In general, these dust curves vary in the slope in the UV/optical range, and the presence (or absence) of a UV bump. It has also been shown that galaxies in the local Universe exhibit a wide range of dust attenuation curves, which can, for instance, be parametrized with the Salim dust curve (Salim, Boquien & Lee 2018). This parametrization is a modified Calzetti curve that allows the slope of the curve to vary, and allows for the presence or absence of a UV bump. Alternative dust attenuation curves include the flexible two-component Charlot & Fall (2000) model, and the Noll et al. (2009) model that modifies the Calzetti curve by including a Lorentzian-like UV bump. The UV bump strength is thought to vary with the slope of the dust attenuation curve, such that flatter attenuation curves display a weaker bump strength (Kriek & Conroy 2013; Narayanan et al. 2018). It must be noted that this correlation is not seen in all studies. For example, Buat et al. (2011, 2012) find no clear relationship between the slope of the attenuation curve and UV bump strength. It has also been suggested that for galaxies with fixed optical depth, galaxies with higher metallicities have flatter attenuation curves but stronger UV bump strengths (Shivaei et al. 2020), indicating a lower prevalence of the dust grains responsible for the UV bump at low metallicity. However, this relationship is not observed universally, with studies such as Salim & Narayanan (2020) suggesting that star–dust geometry and radiative transfer effects can also affect the UV bump strength.

The UV bump is a strong feature seen in the dust attenuation curve of some galaxies, and was first detected in MW sightlines by Stecher (1965). The origin of this feature is not well known (Draine 1989), and was initially suggested to be caused by graphite (Stecher & Donn 1965). Today, this feature is most commonly attributed to nanoparticles containing aromatic carbon (C), such as polycyclic aromatic hydrocarbons (PAHs) (e.g. Joblin, Leger & Martin 1992; Bradley et al. 2005; Shivaei et al. 2022), or nano-sized graphite grains (Li & Draine 2001). Other interpretations, including a random arrangement of microscopic sp^2 carbon chips, have also been proposed (Papoular & Papoular 2009). PAHs are hydrocarbon molecules with C atoms arranged in a honeycomb structure of fused aromatic rings with peripheral H atoms, and are abundant in the ISM (Tielens 2008).

Beyond the local Universe, this feature has only been seen spectroscopically in metal-enriched galaxies at $0.01 \leq z \leq 3$ (e.g. Noll et al. 2007; Noll et al. 2009; Shivaei et al. 2022), and was first seen in a galaxy at $z > 3$ in the spectrum of JADES-GS-z6-0 at $z = 6.71$ (Witstok et al. 2023), with tentative evidence of a higher peak wavelength than that typically observed within the MW, suggesting a differing mixture of carbonaceous grains (Blasberger et al. 2017). The UV bump has since been detected in individual galaxies at redshifts up to $z \sim 7.55$ (Markov et al. 2023, 2025; Fisher et al. 2025) when the Universe was only ~ 700 Myr old. The presence of the UV bump at such early times challenges existing models of dust formation. Asymptotic giant branch (AGB) stars provide a likely origin for PAHs (Latter 1991), and the standard production channel of carbonaceous dust grains is thought to be through low-mass ($\leq 3\,M_\odot$) AGB stars reaching the end of their main-sequence lifetime on time-scales exceeding 300 Myr. If this is the dominant production channel of PAHs, the detection of the UV bump at $z \sim 7$ implies that the onset of star formation occurred at $z \geq 10$ (Witstok et al. 2023). For a galaxy where the onset of star formation occurs at $z = 10$, low-mass AGB stars would begin dust production at $z \sim 7$, so it is expected that supernovae (SNe) instead dominate dust production, with dust-producing SNe II occurring ~ 10 Myr after the onset of star formation (see Schneider & Maiolino 2024 for a review). Supporting the idea of early dust production, enhanced carbon-to-oxygen (C/O) ratios are seen in metal-poor stars in the MW, and have now been observed in GS-z12, a galaxy at $z = 12.5$ (D'Eugenio et al. 2024). While the chemical enrichment pattern of GS-z12 is inconsistent with pure SNe II yields, low-energy Population III SNe yields may explain the C/O lower limit (Vanni et al. 2023; D'Eugenio et al. 2024). Furthermore, it has also been suggested that the slope of the attenuation curve flattens and the strength of the UV bump weakens with increasing redshift due to the grain size distribution changing, with larger dust grains at earlier epochs (Makiya & Hirashita 2022), which could be due to SNe being the prominent channel of dust formation.

The dust attenuation curves of high-redshift galaxies remained largely unconstrained until the launch of the *James Webb Space Telescope* (*JWST*; McElwain et al. 2023; Rigby et al. 2023). With the Near-infrared Spectrograph (NIRSpec; Jakobsen et al. 2022; Böker et al. 2023) onboard *JWST*, we are now able to explore the dust attenuation curves of high-redshift galaxies in more detail with successful detections of the UV bump (Markov et al. 2023, 2025; Witstok et al. 2023) out to redshifts of 8, place constraints on the nebular attenuation curve of a galaxy at $z = 4.41$ (Sanders et al. 2024a), and explore the redshift evolution of dust attenuation curves (e.g. Markov et al. 2025), where it has been suggested that the attenuation curve flattens with increasing redshift independent of A_V.

Here, we combine NIRSpec Wide GTO observations with data from the *JWST*/Near-infrared Camera (NIRCam; Rieke et al. 2023) to investigate the presence of a UV bump in a galaxy at $z = 7.11235$. This system is potentially undergoing a merger, allowing us to explore the implications of these findings for dust formation in the early Universe. This paper is structured as follows: in Section 2 we discuss the observations used in this work, in Section 3 we discuss our methods and analysis, and we place these into the context of galaxy and dust formation in Section 4. Finally, our findings are summarized in Section 5. Throughout this paper, we assume a standard cosmology of $H_0 = 70\ \mathrm{km s^{-1} Mpc^{-1}}$, $\Omega_m = 0.3$, and $\Omega_\Lambda = 0.7$ and a solar abundance of $12 + \log(O/H) = 8.69$ (Asplund, Amarsi & Grevesse 2021). All magnitudes are quoted in the AB magnitude system (Oke & Gunn 1983), and galaxy sizes refer to the half-light radius.

2 OBSERVATIONS

GNWY-7379420231, at $z_{\rm prism} = 7.11235$, was observed as part of the NIRSpec Wide Guaranteed Time Observations (GTO) Program (Maseda et al. 2024, henceforth referred to as Wide). The Wide survey covers the five extragalactic deep fields of the Cosmic Assembly Near-infrared Deep Extragalactic Legacy Survey (CANDELS; Grogin et al. 2011; Koekemoer et al. 2011) with 31 pointings, covering ≈ 320 arcmin^2 in 105 h. As part of the high-priority targets in the Wide survey, IRAC-excess sources from Smit et al. (2015) and Roberts-Borsani et al. (2016) are observed, i.e. galaxies at $z = 6$–8 with strong optical emission lines determined from *Spitzer*/IRAC photometry. At the time of writing, the sample of IRAC-excess sources is made up of 23 galaxies, covering a redshift range of $z = 5.66$–7.65. Through visual inspection of these sources, we identify the presence of a strong UV bump in GNWY-7379420231 only. We show a tentative UV bump detection in EGSZ-9135048459, at $z_{\rm prism} = 6.74$, in Appendix A.

GNWY-7379420231 was originally identified as a Lyman break candidate at $z_{\rm phot} = 8.29$ in Bouwens et al. (2015), and identified as a *Spitzer*/IRAC-excess source in Roberts-Borsani et al. (2016). Subsequent Keck/MOSFIRE observations in Roberts-Borsani et al. (2023) revealed Ly α emission, confirming a spectroscopic redshift of $z_{\rm Ly\alpha} = 7.10813 \pm 0.00019$.

2.1 Spectroscopic observations

The low-resolution spectrum was obtained using PRISM/CLEAR (PRISM hereafter), covering a wavelength range of 0.6–5.3 μm at a spectral resolution of $R \approx 100$ (varying from 30 to 300 for a uniformly illuminated shutter; Jakobsen et al. 2022). High-resolution spectra were obtained using the G235H and G395H gratings (and associated *F170LP* and *F290LP* filters), providing wavelength coverage of 1.66–3.05 μm and 2.78–5.14 μm, respectively, at a spectral resolution of $R \approx 2700$.

For the PRISM spectrum, one exposure with 55 groups was taken, using the NRSIRS2RAPID read-out mode (Rauscher et al. 2017) with a three-point nodding pattern to cycle through the three shutter-slitlet per target. This results in an effective exposure time of 2451 s. The high-resolution gratings were nodded between the two outer shutter positions. For the G235H grating, one exposure with 55 groups was taken for each of the two nodding positions (1634 s total) and for the G395H grating one exposure with 60 groups was taken (1780 s total).

2.2 NIRSpec data reduction

We use the same core reduction process as other NIRSpec Multi-Object Spectroscopy (MOS) GTO surveys (e.g. Cameron et al. 2023; Curtis-Lake et al. 2023; Bunker et al. 2024; Carniani et al. 2024; Saxena et al. 2024b) developed by the ESA NIRSpec Science Operations Team (SOT) and GTO teams, as described in Carniani et al. (2024). Most of the pipeline uses the same algorithms as the official Space Telescope Science Institute (STScI) pipeline (Alves de Oliveira et al. 2018; Ferruit et al. 2022), with small survey-specific modifications (Maseda et al. 2024). We use a finer grid in wavelength with regular steps in the 2D rectification process. We also estimate path losses for each source by taking the relative intra-shutter position into account and assuming a point-like morphology, as in Bunker et al. (2024) and Curti et al. (2024a). The Wide reduction differs from other GTO reductions in the sigma-clipping algorithm used to exclude outliers when creating the 1D spectrum, which does not

work well with a low number of exposures as in Wide, and does not account for Poisson noise from bright pixels, which is typical for many Wide targets. Therefore, the reductions used in this work skip this step.

2.3 NIRCam imaging

We use NIRCam imaging of the Great Observatories Origins Deep Survey (Giavalisco et al. 2004) North (GOODS-N) field, obtained as part of the *JWST* Advanced Deep Extragalactic Survey (JADES; Eisenstein et al. 2023) from programme 1181 (PI: Eisenstein). Nine filters in total are used within these observations: *F090W*, *F115W*, *F150W*, *F200W*, *F277W*, *F335M*, *F356W*, *F410M*, and *F444W*. The reduction of these images closely follows the method used in Rieke et al. (2023).

2.4 Aperture correction

We use NIRCam photometry extracted within Kron apertures with Kron parameter equal to 1.2 ($R_{\rm Kron,s}$) as high signal-to-noise estimates of flux in each filter band. For a galaxy with a Sérsic index of $n = 1$, $R_{\rm Kron,s}$ corresponds to the half-light radius (Graham & Driver 2005). We use the Kron photometry extracted in apertures with Kron parameter equal to 2.5 ($R_{\rm Kron}$) to determine the ratio $R_{\rm Kron}/R_{\rm Kron,s}$ in the *F444W* band to estimate the amount of flux missed by the smaller apertures. We then correct all $R_{\rm Kron,s}$ fluxes by this factor to obtain our final flux values.

In order to correct the spectrum to account for flux outside the slit, we first derive synthetic photometry of the NIRSpec spectrum using the NIRCam filter curves. We then multiply the spectrum by the median ratio of the scaled $R_{\rm Kron,s}$ photometry to the synthetic photometry, excluding *F090W* where the source is not detected. The 1D and 2D spectra are shown in Fig. 1 with the NIRCam photometry and filter curves.

3 METHODS AND ANALYSIS

3.1 Spectroscopic redshift

We estimate the spectroscopic redshift from the PRISM spectrum with msaexp[1] (Brammer 2023) using EAZY templates (Brammer, van Dokkum & Coppi 2008), as in Maseda et al. (2024). From this, we obtain a spectroscopic redshift of $z_{\rm prism} = 7.11235$. We additionally estimate the [O III] $\lambda 5007$ Å redshift from the G395H spectrum, obtaining a redshift of $z_{\rm [O\,III],G395H} = 7.1082^{+0.000040}_{-0.000046}$. Although $z_{\rm [O\,III],G395H}$ is closer to $z_{\rm Ly\alpha}$, we use $z_{\rm prism}$ for all analysis of the NIRSpec PRISM spectrum, and use $z_{\rm [O\,III],G395H}$ for analysis of the high-resolution G395H spectrum.

3.2 UV magnitudes and slopes

We convert the *JWST* NIRCam *F150W* apparent magnitude ($m_{\rm UV}$) to give UV absolute magnitude ($M_{\rm UV}$), which is reported in Table 1. We model the UV continuum slope of the galaxy considered here with a power law $F_\lambda \propto \lambda^\beta$. We measure this slope within the fitting windows defined in Calzetti et al. (1994), following the approach adopted in previous studies (e.g. Austin et al. 2024; Saxena et al. 2024a). We exclude the windows redwards of 1833 Å to exclude the UV bump region and the C III] $\lambda\lambda 1907$, 1909 doublet (C III]). We

---

[1] https://github.com/gbrammer/msaexp
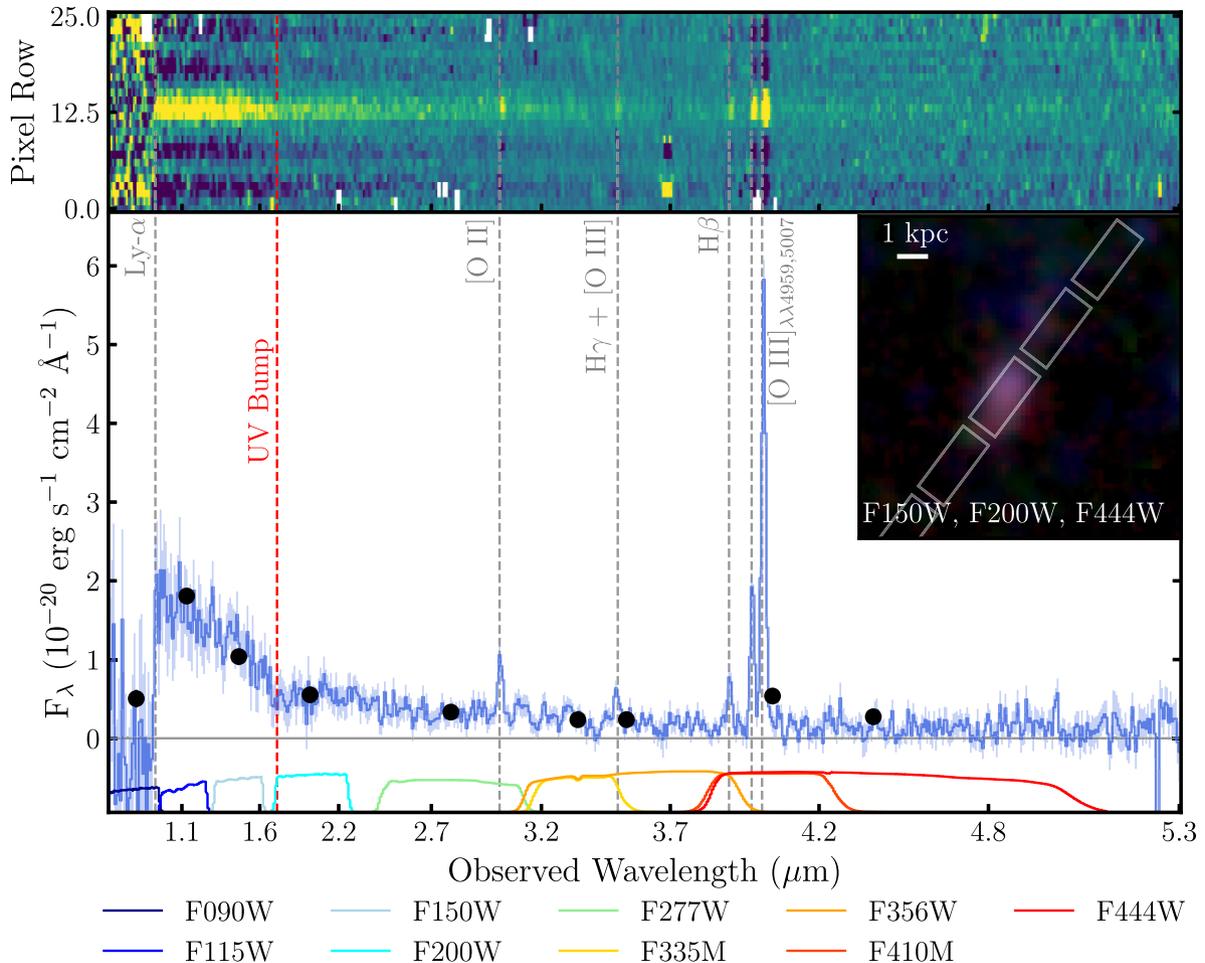
Figure 1. 2D spectrum (top panel) and the 1D spectrum (bottom panel) of GNWY-7379420231 (solid blue line) with photometry overlaid (black points). The location of the 2175 Å UV bump is shown by the dashed red vertical line, and the locations of key emission lines are shown by dashed grey lines. The transmission curves for each photometric filter used are also shown. The inset panel shows a PSF-matched RGB image of GNWY-7379420231 (R: *F444W*, G: *F200W*, B: *F150W*) with the location of the NIRSpec slitlets outlined in solid white lines.

include a fitting window at 2580–2640 Å to reduce the uncertainty on the fit.

We use a Bayesian fitting procedure to fit the rest-frame UV continuum using a PYTHON implementation of the MULTINEST nested sampling algorithm (Feroz, Hobson & Bridges 2009), PYMULTINEST (Buchner et al. 2014). We use a Gaussian prior distribution for the power-law index, centred on $\mu_\beta = -2$, with a standard deviation of $\sigma_\beta = 0.5$. This is motivated by studies such as Austin et al. (2024) and Saxena et al. (2024a), which find that the average UV continuum slope at $z \sim 7$ is $\beta_{\rm UV} \sim -2$. We use a flat prior on the normalization at $\lambda_{\rm rest} = 1500$ Å (between 0 and twice the maximum flux value of the spectrum in the fitting regions). The best-fitting value of β is given by the 50th percentile (median) of the posterior distribution, with the 16th and 84th percentiles given as a $\pm 1\sigma$ confidence range. The UV slope fit is shown in Fig. 2.

3.3 UV bump identification

To determine the robustness of the UV bump feature, we follow the method defined in Witstok et al. (2023). We fit power laws in four adjacent wavelength windows defined by Noll et al. (2007), with power-law indices γ_1 to γ_4. While the γ_3 region begins at 1920 Å

in Noll et al. (2007), we exclude the region 1920 Å $< \lambda_{\rm emit} < 1950$ Å to ensure we avoid contamination from the C III] doublet. The parameter $\gamma_{34} \equiv \gamma_3 - \gamma_4$ is used to identify the presence of the absorption feature centred on 2175 Å, where a more prominent UV bump being present results in a more negative value of γ_{34} (Noll et al. 2009). Prior to fitting the wavelength windows, the spectrum is smoothed with a running median filter of 15 pixels. The uncertainty of the running median is estimated with a bootstrapping procedure, where each of the 15 pixels is randomly perturbed according to their formal uncertainty for 100 iterations.

We choose flat prior distributions for the power-law indices within the range $-10 < \gamma_i < 1$, and normalize at the centre of each wavelength window, between 0 and twice the maximum value of the flux in each fitting region. The best-fitting value of γ_{34} is given by the median of the posterior distribution obtained by simultaneously fitting γ_3 and γ_4, with the 16th and 84th percentiles given as a $\pm 1\sigma$ confidence range.

3.4 UV bump fitting

As in Witstok et al. (2023), we parametrize the UV bump profile by defining the excess attenuation as $A_{\lambda,\,\rm bump} =$

**Table 1.** The properties of GNWY-7379420231. Error bars represent 1σ uncertainties.

Parameter	Value
Wide ID	2008001576
RA	12:37:37.941
Dec.	+62:20:22.850
z_{prism}	7.11235
$z_{[O III],G395H}$	$7.1082^{+0.000040}_{-0.000046}$
M_{UV} (mag)	-20.29
β_{UV}	-1.81 ± 0.24
γ_{34}	$-6.58^{+1.85}_{-1.69}$
$A_{\lambda,max}$ (mag)	$0.46^{+0.06}_{-0.07}$
λ_{max} (Å)	2257^{+26}_{-28}
[O III] + Hβ EW$_0$ (Å)	1110 ± 183
$\log_{10}$(O32)	0.39 ± 0.19
$\log_{10}$(R23)	1.23 ± 0.24
$\log_{10}$(R2)	0.59 ± 0.29
$\log_{10}$(R3)	0.98 ± 0.25
$\hat{R}$	1.14 ± 0.26
Z_{neb} ($Z_\odot$)	$0.30^{+0.10}_{-0.09}$
$\log_{10}(n_e)$ (cm^{-1})	$3.12^{+0.83}_{-0.47}$
$\log_{10}(M_{dyn}/M_\odot)$	9.35 ± 0.43

$-2.5 \log_{10}\left(F_\lambda / F_{\lambda, \text{cont}}\right)$, where F_λ is the observed flux, and $F_{\lambda, \text{cont}}$ is the UV continuum slope, without a UV bump (Shivaei et al. 2022). We use the running median and its corresponding uncertainty (see Section 3.3) to compute the significance of the negative flux excess of the spectrum with respect to the power-law UV slope (β_{UV}), determined in Section 3.2.

We use the MULTINEST nested sampling algorithm to fit the excess attenuation $A_{\lambda, \text{bump}}$ with a Drude profile (Fitzpatrick & Massa 1986). The Drude profile is characterized by the parameters $A_{\lambda,max}$, the peak amplitude of the bump; λ_{max}, the rest-frame central wavelength of the bump; and γ, which is related to the full width at half-maximum (FWHM) as FWHM$= \gamma \lambda_{max}^2$. The Drude profile is then defined as

$$A_{\lambda, \text{bump}} = A_{\lambda,max} \frac{\gamma^2/\lambda^2}{\left(1/\lambda^2 - 1/\lambda_{max}^2\right)^2 + \gamma^2/\lambda^2}. \quad (1)$$

We fix $\gamma = 250 \, \text{Å}/(2175 \, \text{Å})^2$, which corresponds to FWHM$= 250$ Å if $\lambda_{max} = 2175$ Å, in agreement with findings for $z \sim 2$ star-forming galaxies (Noll et al. 2009; Shivaei et al. 2022). We note that allowing the FWHM to vary does not affect the other parameters. We carry out the fitting procedure in a region of $1950 \, \text{Å} < \lambda_{emit} < 2580 \, \text{Å}$, which includes the γ_3 and γ_4 regions, but excludes the C III] doublet. As in Witstok et al. (2023), we use a gamma distribution with shape parameter $a = 1$ and scale $\theta = 0.2$ as a prior for bump amplitude, $A_{\lambda,max}$. This prior is chosen as it favours lower amplitudes, consistent with our expectations for high-redshift galaxies (e.g. Markov et al. 2025), although a flat prior gives comparable results. We use a flat prior for the central wavelength in the range $2100 \, \text{Å} < \lambda_{max} < 2300$
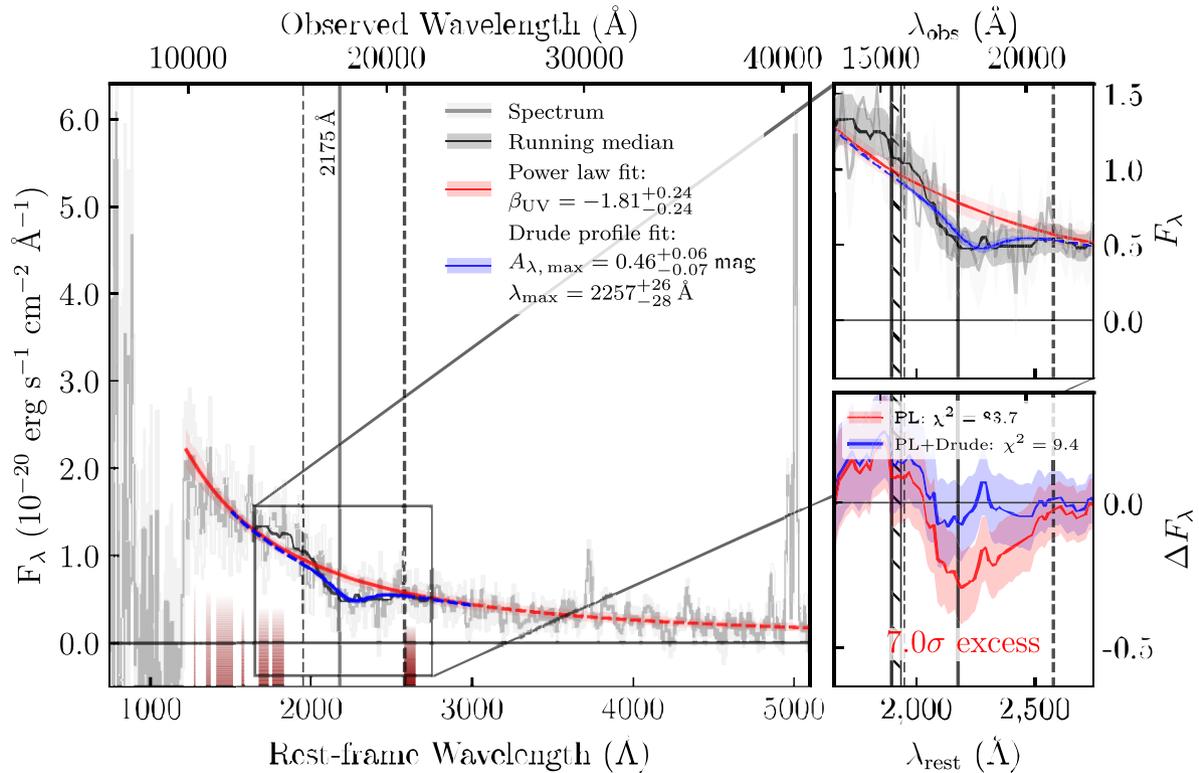
Figure 2. Spectrum of GNWY-7379420231 (grey solid line) with a power-law fit to the UV continuum (red solid line). The dark red shading represents the UV slope fitting windows. The zoom-in panel of the region around 2175 Å shows the running median, indicated by a solid black line. This represents the attenuated stellar continuum, and shows a localized absorption feature. The Drude profile fit is shown by the solid blue line, within the fitting window indicated by the vertical dashed lines. The hatched region shows the location of the C III doublet. The bottom right panel shows the residuals of the power-law fit (PL) and the combined power-law and Drude profile fit (PL + Drude). The power-law fit alone has a 7.0σ negative flux excess, with the PL + Drude model showing a significantly better fit, as supported by the BIC values.

Å. The UV bump fit is shown in Fig. 2, with best-fitting values listed in Table 1. We compare this model to a simple power law using the Bayesian Information Criterion (BIC). The significantly lower BIC value for the UV bump model (ΔBIC = 66.7) indicates that this model is preferred over a simple power-law model.

3.5 SED fitting

We model the SED of GNWY-7379420231 using BAGPIPES (Bayesian Analysis of Galaxies for Physical Inference and Parameter EStimation; Carnall et al. 2018, 2019), fitting both the photometry and spectroscopy simultaneously. We use Binary Population and Spectral Synthesis (BPASS) v2.2.1 models (Stanway & Eldridge 2018), with models that include binary stars. We use the default BPASS initial mass function '135_300' (IMF; stellar mass from $0.1 M_\odot$ to $300 M_\odot$ and a slope of -2.35 for $M > 0.5 M_\odot$). We mask the region around Ly α (1200 Å $< \lambda_{\rm emit} <$ 1250 Å) to mitigate any potential effects from Lyman α damping-wing absorption. We also mask the region 4900 Å $< \lambda_{\rm emit} <$ 5100 Å in the spectrum due to small discrepancies between the [O III] equivalent widths (EWs) in the spectroscopy and photometry. While BAGPIPES can account for small wavelength-dependent variations between the spectroscopy and photometry, it is not flexible enough to solve for emission-line discrepancies. We have verified that the SED fitting results do not change significantly if the spectrum is left unmasked.

We assume a non-parametric star formation history (SFH) from Leja et al. (2019), which fits the star formation rates (SFRs) in fixed time bins, where ΔlogSFR between bins is linked by a Student's t-distribution. As in Tacchella et al. (2022), we fit a 'continuity' model, with $\sigma = 0.3$ and $\nu = 2$, which is weighted against rapid transitions in SFR, and a 'bursty continuity' model with $\sigma = 1$ and $\nu = 2$, which allows more variation in SFR (i.e. a more bursty SFH). We fix the redshift of the galaxy to $z_{\rm prism} = 7.11235$, and fit the SFH in six bins of lookback time t, with the first bins fixed to 0 Myr $< t <$ 3 Myr and 3 Myr $< t <$ 10 Myr, motivated by observational evidence for bursty SFHs seen at high redshift (e.g. Boyett et al. 2024; Endsley et al. 2025; Looser et al. 2025) and following the same approach adopted by Whitler et al. (2023). The remaining four bins are equally log-spaced in lookback time until $t(z = 20)$. We note that the inferred SFH is largely insensitive to the number of bins used as long as $N_{\rm bins} \geq 4$ (Leja et al. 2019). We favour the 'bursty continuity' model as this flexible SFH accommodates both stochastic star formation and underlying older stellar populations. It should be noted that this model still allows smooth or declining SFHs if favoured during the fitting (see Harvey et al. 2025). We reduce the star formation time-scale to 10 Myr to account for the increased specific star formation rate (sSFR), compared to galaxies at lower redshift.

The allowed total stellar mass formed and stellar metallicities are allowed to vary uniformly between 10^5 M$_\odot <$ M$_\star < 10^{12}$ M$_\odot$, and $0 < Z_* < 0.5$ Z$_\odot$, respectively. Nebular emission is included using a grid of CLOUDY (Ferland et al. 2017) models, parametrized by the ionization parameter ($-3 < \log_{10}$U < -0.5), which BAGPIPES computes self-consistently. We use the Salim et al. (2018) dust attenuation curve, which parametrizes the dust curve shape with a power-law deviation δ from the Calzetti et al. (2000) model ($\delta = 0$ for the Calzetti curve) and includes a Drude profile to model the 2175 Å bump. The strength of the bump is given by the amplitude B, in units of $A_{\rm bump}/E(B - V)$, where $A_{\rm bump}$ is the extra attenuation at 2175 Å. We keep the central wavelength and width of the bump fixed at 2175 and 250 Å, respectively. We use uniform priors for δ ($-0.5 < \delta < 0.2$, adapted from Kriek & Conroy 2013) and B ($0 < B < 10$). Following Witstok et al. (2023), we use

Table 2. Best-fitting values for the physical properties of GNWY-7379420231 from SED fitting with differing dust attenuation curves. The first row contains the 10 Myr SFRs, the second row provides the mass weighted ages, the third row gives the stellar metallicity, the fourth row the stellar mass, the fifth row the ionization parameter, and the final row gives the V-band dust attenuation. All errors are the 16th and 84th percentiles of the posterior distribution.

| Parameter	Salim	Li	MW	Salim ($B = 0$)
SFR$_{10}$ (M$_\odot$ yr^{-1})	$15.5^{+7.4}_{-5.2}$	$24.7^{+7.0}_{-8.5}$	$16.2^{+7.5}_{-4.8}$	$11.3^{+4.5}_{-3.2}$
t_* (Myr)	59^{+125}_{-42}	22^{+61}_{-16}	39^{+85}_{-24}	166^{+105}_{-99}
$Z_\star$(Z$_\odot$)	$0.27^{+0.06}_{-0.05}$	$0.29^{+0.06}_{-0.06}$	$0.32^{+0.03}_{-0.03}$	$0.32^{+0.08}_{-0.10}$
$\log_{10}(M_\star/\mathrm{M}_\odot)$	$8.60^{+0.15}_{-0.13}$	$8.57^{+0.13}_{-0.10}$	$8.63^{+0.13}_{-0.12}$	$8.84^{+0.13}_{-0.15}$
$\log_{10}U$	$-1.73^{+0.15}_{-0.15}$	$-1.76^{+0.17}_{-0.17}$	$-1.77^{+0.16}_{-0.15}$	$-1.83^{+0.15}_{-0.13}$
A_V (mag)	$0.27^{+0.06}_{-0.05}$	$0.40^{+0.05}_{-0.06}$	$0.32^{+0.03}_{-0.03}$	$0.31^{+0.08}_{-0.10}$

a Gaussian prior on the V-band dust attenuation with $\mu_{A_V} = 0.15$ mag, $\sigma_{A_V} = 0.15$ mag, and attenuation limited to $0 < A_V < 7$ mag, fixing the fraction of attenuation arising from stellar birth clouds to 60 per cent, with the remaining 40 per cent coming from the diffuse ISM (Chevallard et al. 2019). We also assume a log-prior on the velocity dispersion in the range 1–1000 km s^{-1}. Finally, we assume that the spectrum follows the PRISM resolution curve based on a point-source morphology, using the resolution curve of an idealized point source generated with msafit, as described in de Graaff et al. (2024a, Appendix A).

We carry out further BAGPIPES fits, varying only the assumed dust attenuation curve. We perform fits with the MW dust curve, the Salim dust law with B fixed as 0 (henceforth referred to as the flat Salim curve), allowing only the slope (δ) to deviate from the Calzetti curve, and the Li et al. (2008) analytical expression for the dust attenuation law, used in Markov et al. (2023, 2025). This dust parametrization has the benefit of allowing SED fitting to be carried out without assuming the prior shape of the dust curve, but has the disadvantage of having four free parameters, thus should only be used with spectroscopic data, or photometric surveys with a sufficiently large number of photometric bands (Markov et al. 2023). We modify the expression to allow for a variable width of the Drude profile characterizing the UV bump, and as such the dust curve, normalized to the attenuation at 0.55 μm (A_V), is given by

$$A_\lambda/A_V = \frac{c_1}{(\lambda/0.08)^{c_2} + (0.08/\lambda)^{c_2} + c_3}$$
$$+ \frac{233\,[1 - c_1/(6.88^{c_2} + 0.145^{c_2} + c_3) - c_4/x]}{(\lambda/0.046)^2 + (0.046/\lambda)^2 + 90}$$
$$+ \frac{c_4}{(\lambda/0.2175)^2 + (0.2175/\lambda)^2 + [(w/0.2175)^2 - 2]}, \quad (2)$$

where c_1, c_2, c_3, and c_4 are dimensionless parameters, λ is the wavelength in μm, $x = (6.55 + [(w/0.2175)^2 - 2])$, and w is the width of the UV bump in μm. The three terms of equation (2) describe the FUV rise, the optical and near-infrared (NIR) attenuation, and the 2175 Å UV bump. We use priors for $c_1 - c_4$ adapted from those given in Markov et al. (2025), requiring $c_4 \geq 0$, and set $w = 0.0250$ μm. We present the best-fitting values obtained with each dust curve, along with 1σ errors in Table 2. We summarize the priors used in Table B1. The posterior spectra and dust curves are shown in Fig. 3. We show the full posterior spectra with residuals in Fig. B1.

We find that fitting the photometry or spectrum alone recovers similar parameters for the UV bump (see Fig. B2).
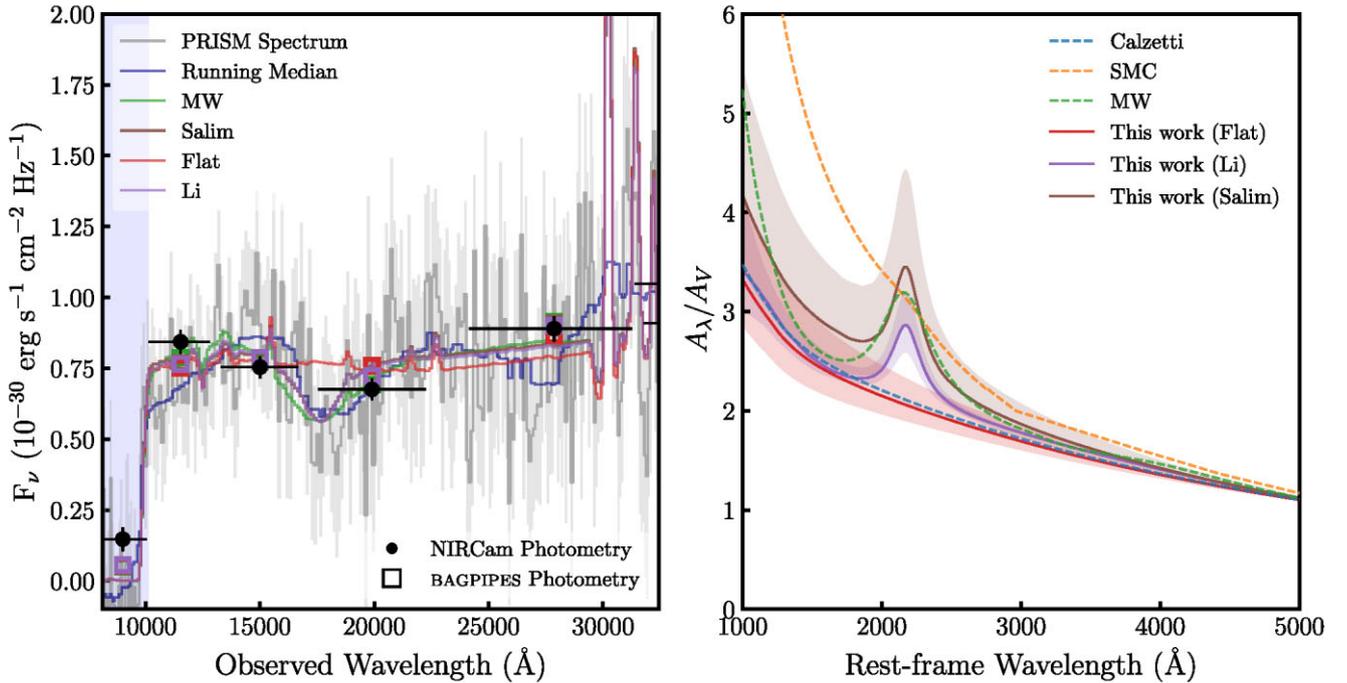
Figure 3. Left: posterior spectra obtained from combined BAGPIPES fitting of the photometry and spectroscopy. The observed spectrum and associated errors are shown in grey, while the running median is shown in dark blue. The x error bars represent the width of the filter at 50 per cent of the maximum transmission. The blue shading shows the spectral regions masked in the fitting process. Right: the best-fitting dust attenuation curve obtained from our BAGPIPES fit with the Salim dust curve is shown by the solid brown line, with the brown shaded region showing the 1σ uncertainty. The best-fitting Li model and 1σ uncertainty is shown by the solid purple line, and purple shading, and the red solid line represents the best-fitting dust attenuation curve from the flat Salim fit. We show the Calzetti, MW, and SMC curves for comparison, in the blue, orange, and green dashed lines, respectively.

3.6 Morphology

We perform surface brightness fitting with GALFIT version 3.0.5 (Peng et al. 2002, 2010) to investigate the morphology of our source. GALFIT convolves the galaxy surface brightness profile with a point spread function (PSF), and uses the Levenberg–Marquardt algorithm to minimize the χ^2 of the fit.

We create PSF-matched images using APERPY[2] (Weaver et al. 2024), which creates empirical PSFs and makes use of PYPHER (Boucaud et al. 2016) to create PSF-matched kernels. We create a PSF-matched stack of the filters in the short-wavelength (SW) channel where the source is detected (*F115W*, *F150W*, *F200W*) to determine the components required for fitting.

We fit the source using two Sérsic components and a point source. The Sérsic profile has the form

$$I(R) = I_e \exp\left\{-b_n\left[\left(\frac{R}{R_e}\right)^{1/n} - 1\right]\right\}, \qquad (3)$$

where $I(R)$ is the intensity at a distance R from the centre of the galaxy, R_e is the half-light radius of galaxy, I_e is the intensity at the half-light radius, n is the Sérsic index (Sérsic 1963; Ciotti 1991; Caon, Capaccioli & D'Onofrio 1993), and b_n can be approximated as $b_n \approx 2n - \frac{1}{3} + \frac{4}{405n} + \frac{46}{25515n^2}$ (Ciotti & Bertin 1999). We allow R_e, magnitude, axis ratio (b/a), and position angle to vary freely, allow the Sérsic index to vary in the range $0 < n < 10$, and allow the source position to vary within ± 3 pixels of the input location in
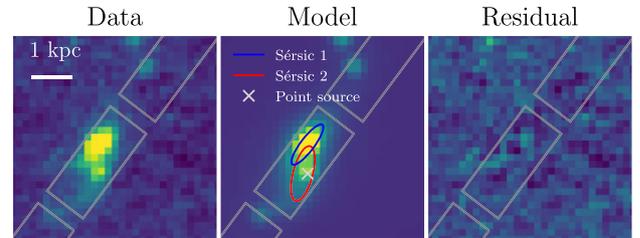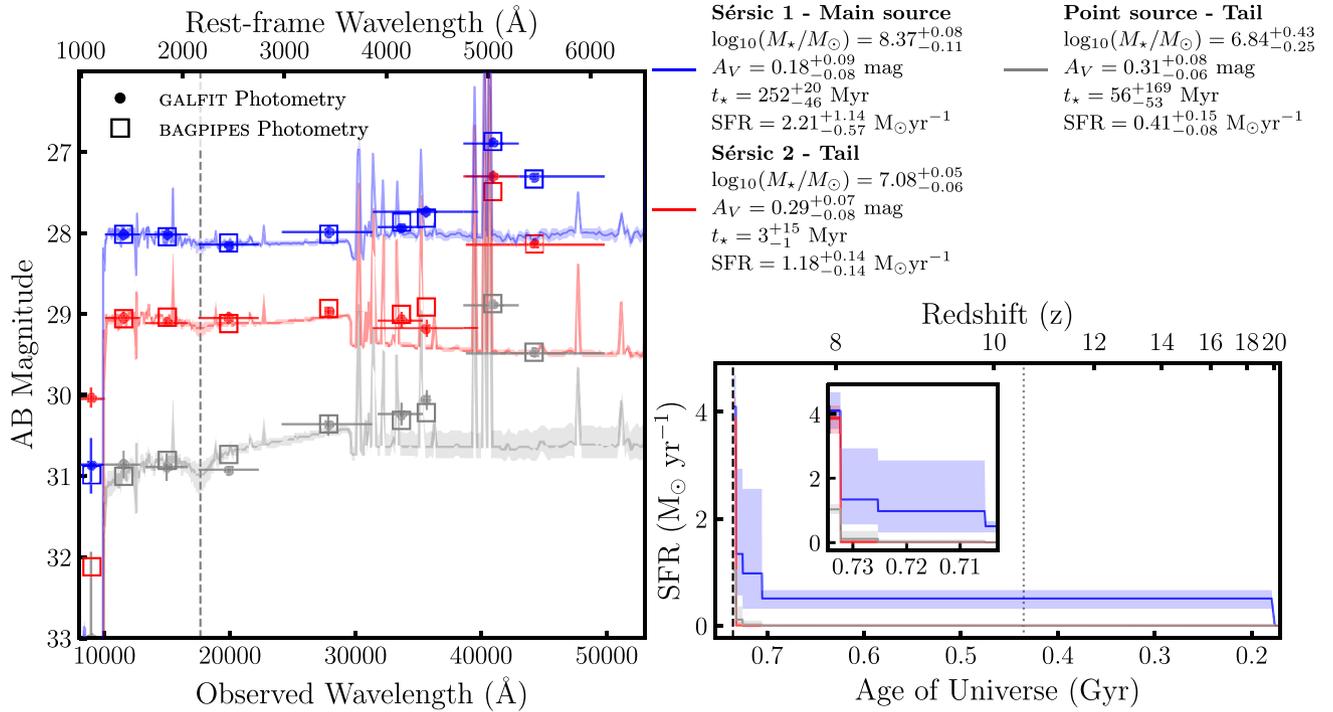

Figure 4. Left: the stacked data image provided as input to GALFIT. Middle: the GALFIT model image. The two Sérsic profiles are shown by the blue and red ellipses, with the point source indicated by the grey cross. Right: the residual image, created by subtracting the model image from the data image. The data and model images are linearly scaled between -3σ and -20σ of the data image background, and the residual image is scaled between -3σ and -10σ of the data image background, for clarity. The location of the NIRSpec slitlets are overplotted in grey.

both the x and y direction. We find that one component has a very low Sérsic index, which we fix as $n = 0.2$. The best-fitting model for the SW stack is shown in Fig. 4. We then fit each band individually, keeping all parameters fixed to the best-fitting values while allowing only the magnitude to vary. The best-fitting models are shown in Fig. C1, where the point source component is particularly visible in the SW channels.

The best-fitting model is made up of a main brighter component (Sérsic 1), with a 'tail', made up of the secondary Sérsic component (Sérsic 2) and a point source. The bright region (Sérsic 1) is best fit by a Sérsic profile with $n = 6.04 \pm 2.27$, and has a half-light radius

---

[2] aperpy is available though Github (https://github.com/astrowhit/aperpy) and Zenodo (https://doi.org/10.5281/zenodo.8280270).

Figure 5. Left: posterior spectrum for each component obtained through BAGPIPES SED fitting with 1σ errors. The GALFIT photometry is shown by the solid circles, with the BAGPIPES photometry shown by the open squares. The x error bars show the filter width at 50 per cent of the maximum transmission. Right: the posterior SFH for each component. The grey dotted line indicates where stars would have time (300 Myr) to evolve off the main sequence into an AGB star. The inset panel shows a zoom-in of the three most recent bins of the posterior SFH.

of $R_e = 569 \pm 170$ pc. The fainter Sérsic component (Sérsic 2) is the component that is fit with a fixed Sérsic index of $n = 0.20$, and has a half-light radius of $R_e = 648 \pm 80$ pc. Errors are the 1σ uncertainties derived by GALFIT.

We carry out photometric SED fitting for each of these three components, with the magnitudes obtained from the GALFIT fit in each band. As in Section 3.5, we use BPASS v2.2.1 models with the default BPASS IMF. We keep the redshift of the source fixed and use a 'bursty continuity' model of SFH, with bins of 0–3, 3–10, 10–30, and $30 - t(z = 20)$ Myr. The ionization parameter and metallicity are fixed to the best-fitting values obtained with the Salim dust law in Section 3.5. We use the Salim dust law where the prior on B is a truncated Gaussian prior with $\mu_B = 0$, $\sigma_B = 2$, and $0 < B < 10$. The best-fitting spectra and photometry are shown in Fig. 5, along with the posterior SFHs.

Finally, we use STATMORPH (Rodriguez-Gomez et al. 2019) to measure the Gini-M_{20} statistics, which can be used to quantify galaxy morphology (Lotz, Primack & Madau 2004; Lotz et al. 2008). The Gini coefficient (G) is a statistic that is commonly used in economics to measure wealth distribution in human populations, but was first used by Abraham, van den Bergh & Nair (2003) to provide a quantitative measure of the distribution of light within a galaxy. G is determined from the distribution of the absolute flux values:

$$G = \frac{1}{\overline{|X|}n(n-1)} \sum_i^n (2i - n - 1) |X_i|,$$ (4)

where $\overline{|X|}$ is the mean of the absolute values $|X_i|$ (Lotz et al. 2004; Rodriguez-Gomez et al. 2019). The M_{20} statistic is defined as the normalized second-order moment of the brightest 20 per cent of the galaxy's flux. M_{20} traces the spatial extent of the brightest pixels in

a galaxy, and is defined as

$$M_{20} \equiv \log_{10} \left(\frac{\sum_i M_i}{M_{tot}} \right), \quad \text{while} \quad \sum_i f_i < 0.2 f_{tot},$$ (5)

where M_{tot} is defined as

$$M_{tot} = \sum_i^n M_i = \sum_i^n f_i \left[(x_i - x_c)^2 + (y_i - y_c)^2 \right],$$ (6)

where x_c, y_c is the galaxy's centre, such that M_{tot} is minimized (Lotz et al. 2004; Lotz et al. 2008). We show the location of GNWY-7379420231 on the Gini-M_{20} parameter space in Fig. C2, adopting the classifications from Lotz et al. (2008). Gini and M_{20} can be used to determine whether a galaxy is a merger, if the following criterion is met:

$$G > -0.14 M_{20} + 0.33.$$ (7)

Based on these diagnostics, GNWY-7379420231 falls within the merger region of the parameter space. The stellar mass ratio of 12:1 between Sérsic 1 and the two other components, derived from BAGPIPES spectral fitting, classifies this system as a minor merger. We also see evidence for a minor merger in the G395H 2D spectrum of the [O III] doublet, with a velocity offset of ~ 180 km s^{-1}, shown in Fig. C3.

3.7 Resolved SED fitting

We create PSF-matched images following the same method used in Section 3.6. We choose to match to the $F444W$ mosaic as this has the broadest PSF of our filters. We create an inverse variance weighted stacked image of our source and use VORBIN (Cappellari & Copin 2003) to perform adaptive spatial noise binning to create bins with
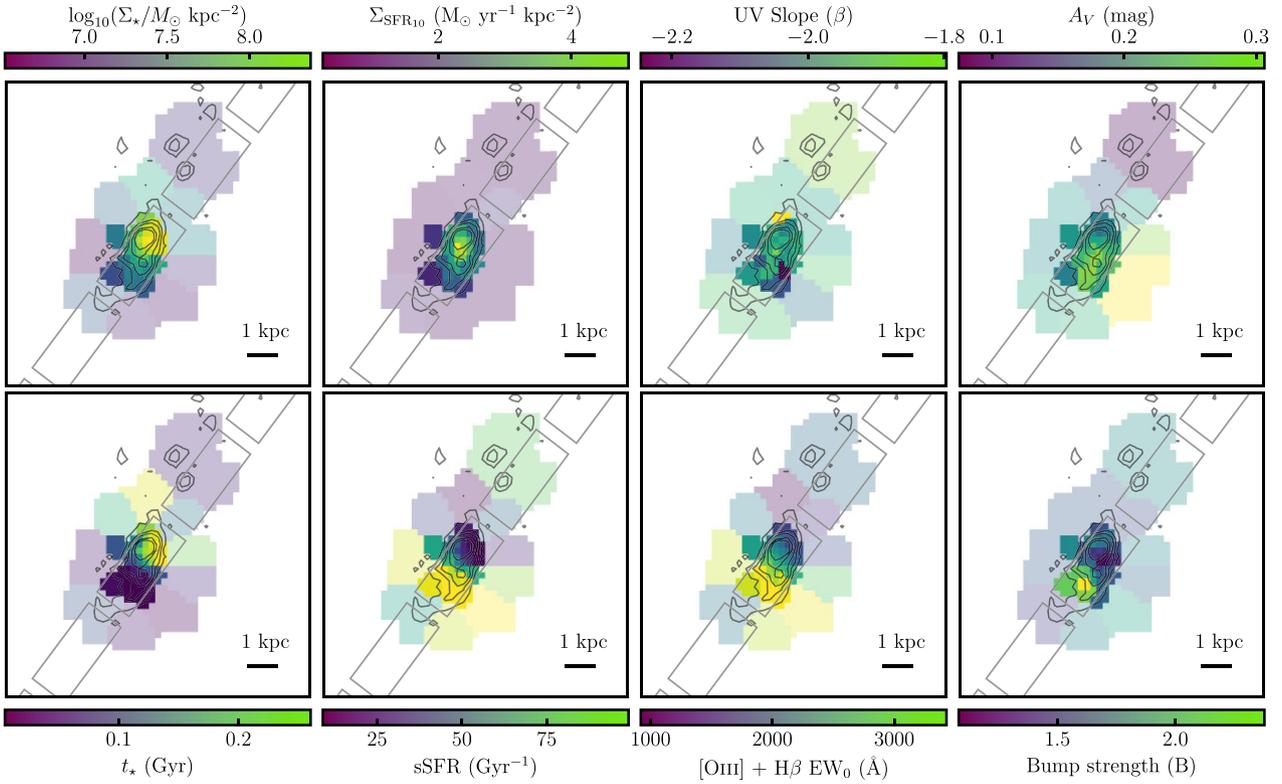
Figure 6. Maps of GNWY-7379420231. Top, from left to right: stellar mass surface density ($\Sigma_\star$), SFR surface density ($\Sigma_{\mathrm{SFR}_{10}}$), UV continuum slope, and *V*-band dust attenuation. Bottom, from left to right: mass-weighted age, sSFR, [O III] + Hβ rest-frame EW, and the UV bump strength (*B*) obtained from the Salim dust law (see Section 3.5). The black lines show the 3σ, 6σ 9σ 15σ, and 21σ contours of the SW stack. The location of the NIRSpec slitlets are overlaid in grey. The fainter bins are those where the photometry has at least one band with SNR< 5 (excluding *F*090*W*).

a target signal-to-noise ratio (SNR) of 25. We extract photometry in each NIRCam filter for each bin, and model the SED of each bin using BAGPIPES.

We apply the same BAGPIPES fitting procedure described in Section 3.6. We again adopt the Salim dust law with a truncated Gaussian prior on *B* ($\mu_B = 0$, $\sigma_B = 2$, $0 < B < 10$) to allow us to trace the location of the UV bump. Using the 50th percentile of the posterior BAGPIPES distributions, we create 2D maps of the physical properties of our source, as shown in Fig. 6. We measure the [O III] + Hβ rest-frame EW from the 50th percentile of the posterior spectrum generated in the fitting process, and measure the UV β slopes using the same fitting windows as in Section 3.2.

3.8 Emission-line measurements

We perform emission-line fitting that accounts for both the line spread function (LSF) broadening and its undersampling by the NIRSpec detectors. It is important that this is accounted for, as fitting a Gaussian to an undersampled line could severely overestimate or underestimate the line flux (de Graaff et al. 2025). To address this, we create Gaussian models on an oversampled grid and convolve them with the LSF of an idealized point source from de Graaff et al. (2024a). We use the MULTINEST nested sampling algorithm to fit the emission lines in both the PRISM and G395H spectra.

We fit the following emission lines in the PRISM spectrum: [O II] λ3727, [O II] λ3729, Hβ, [O III] λ4959, and [O III] λ5007. Due to the resolution of the PRISM spectrum, we fit the blended

[O II] λ3727 + [O II] λ3729 emission lines as a single Gaussian. To reduce the number of free parameters, we fix the central wavelength of each Gaussian profile, and fix the flux ratio of the [O III] $\lambda\lambda$4959, 5007 doublet to the theoretical value of 2.98. As Hα falls outside of the PRISM wavelength range, we instead estimate the dust attenuation from the value of A_V obtained from SED fitting assuming the Salim dust law. We note this is in good agreement with that obtained from the Meurer, Heckman & Calzetti (1999) relation. We convert this to a nebular A_V following Reddy et al. (2020) and correct for dust attenuation assuming the Cardelli et al. (1989) attenuation curve.

The dust-corrected emission-line fluxes are reported in Table D1 as the median of the posterior flux distribution, with errors given as the semidifference of the 16th–84th percentiles of the posterior distribution. As [O III] λ4363 is blended with Hγ in the PRISM spectrum and falls within the chip-gap in the G395H spectrum, we are unable to derive the metallicity of GNWY-7379420231 using the direct-T_e method (e.g. Sanders et al. 2024b). Therefore, we derive the oxygen abundance (12 + log(O/H)) from a range of emission-line ratios:

$$R2 = \log\left(\frac{[\mathrm{O\,II}]\lambda\lambda3727, 3729}{\mathrm{H}\beta}\right) \tag{8}$$

$$O32 = \log\left(\frac{[\mathrm{O\,III}]\lambda5007}{[\mathrm{O\,II}]\lambda\lambda3727, 3729}\right) \tag{9}$$

$$R3 = \log\left(\frac{[\mathrm{O\,III}]\lambda5007}{\mathrm{H}\beta}\right) \tag{10}$$
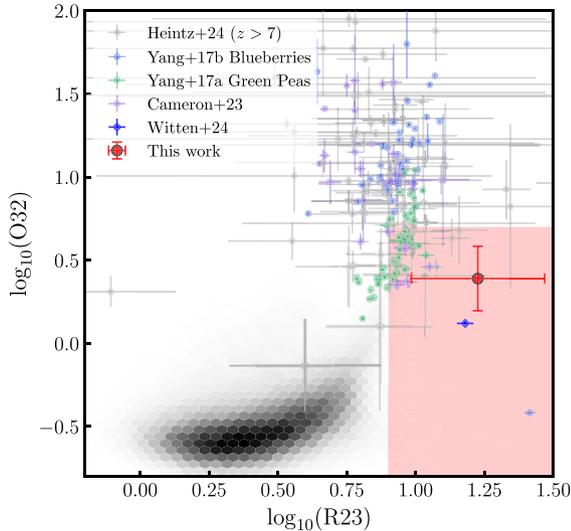
Figure 7. Dust-corrected O_{32}–R_{23} plot, showing GNWY-7379420231 compared to NIRSpec data (Cameron et al. 2023; Heintz et al. 2025; Witten et al. 2025), local analogues (Yang et al. 2017a; Yang et al. 2017b), and the Sloan Digital Sky Survey (York et al. 2000) Data Release 7 (Abazajian et al. 2009), shown in black. The red shading shows the region $\log_{10} O32 < 0.7$ and $\log_{10} R23 > 0.9$, which may contain galaxies hosting an older stellar population (Witten et al. 2025).

$$R23 = \log \left(\frac{[\text{O \sc{II}}]\lambda\lambda 3727, 3729 + [\text{O \sc{III}}]\lambda\lambda 4959, 5007}{\text{H}\beta} \right) \quad (11)$$

$$\hat{R} = 0.47 \times R2 + 0.88 \times R3. \quad (12)$$

Fig. 7 shows the dust-corrected O32 and R23 emission-line ratios. The dust-corrected emission-line ratios are reported in full in Table 1, along with the rest-frame EW of the [O \sc{III}] $\lambda\lambda 4959, 5007$ doublet and H β line. These EWs are obtained using continuum fits from PPXF (Cappellari 2017, 2023), which will be described in Ormerod et al. (in preparation). We combine the information from the emission-line ratios and use the calibrations from Curti et al. (2024b) to calculate the gas-phase metallicity (Z_{neb}) in units of solar metallicity ($Z_\odot$), which is given in Table 1.

Using the $R \sim 2700$ G395H grating, we measure the [O \sc{II}] $\lambda\lambda 3727,3729$ and [O \sc{III}] $\lambda\lambda 4959,5007$ emission lines. We first measure the [O \sc{III}] doublet with tied line widths. We use the median width of the posterior distribution as a fixed width when fitting the [O \sc{II}] doublet, where we also keep the central wavelengths fixed. The [O \sc{II}] fit is shown in Fig. D1.

3.9 Electron density measurement

Electron densities in H \sc{II} regions are crucial for characterizing the ISM, as along with ISM pressure, they govern the emission from H \sc{II} regions (e.g. Kewley et al. 2019b; Isobe et al. 2023; Abdurro'uf et al. 2024). To derive the electron density, we utilize the density-sensitive [O \sc{II}] $\lambda 3726,\lambda 3729$ emission-line ratio (Kewley, Nicholls & Sutherland 2019a), measured from the G395H grating.

We then use PYNEB (Luridiana, Morisset & Shaw 2015) to determine n_e from the [O \sc{II}] line ratio. We adopt an electron temperature of $T_e = 10\,000$ K (e.g. Li et al. 2025); however assuming an electron temperature of 15 000 or 20 000 K has minimal impact on our derived electron density, consistent with the findings by Topping et al. (2025). From this, we obtain a value of $\log_{10}(n_e)$ cm^{-1} = $3.12^{+0.83}_{-0.47}$, in

agreement with the median value determined in Isobe et al. (2023) for $z \sim 7$–9 galaxies.

3.10 Dynamical mass

We follow the method described in Kohandel et al. (2019) to estimate the dynamical mass of our source, which we summarize here. Assuming a rotating disc geometry with radius R, the dynamical mass can be estimated as

$$M_{\text{dyn}} = \frac{v_c^2 R}{G}, \quad (13)$$

where v_c can be estimated from the FWHM of the [O \sc{III}] $\lambda 5007$ emission line using

$$\text{FWHM} = \gamma v_c \sin\theta, \quad (14)$$

where γ is a factor dependent on geometry, line profile, and turbulence. As in Capak et al. (2015), we estimate $\gamma = 1.32$ and additionally include a systematic error on γ of 20 per cent. It is important to note that both Capak et al. (2015) and Kohandel et al. (2019) derive dynamical masses using the [C \sc{II}] 158 µm emission line, rather than the [O \sc{III}]$\lambda 5007$ line employed in this analysis. Dynamical masses derived from the [O \sc{III}]$\lambda 5007$ emission line could be overestimated compared to those derived from cold gas tracers (Kohandel et al. 2024). We determine the inclination (θ) from the axis ratio of Sérsic 1 measured in Section 3.6 using the Hubble (1926) equation

$$\cos^2(\theta) = \frac{(b/a)^2 - (b/a)_{\text{min}}^2}{1 - (b/a)_{\text{min}}^2}, \quad (15)$$

where $(b/a)_{\text{min}} = 0.15$ (e.g. Guthrie 1992; Yuan & Zhu 2004; Sargent et al. 2010; Leslie et al. 2018). Using equations (13) and (14), the general expression for the dynamical mass is

$$M_{\text{dyn}} = 2.35 \times 10^9 M_\odot \left(\frac{1}{\gamma^2 \sin^2\theta} \right) \left(\frac{\text{FWHM}}{100 \text{ km s}^{-1}} \right)^2 \left(\frac{R}{\text{kpc}} \right). \quad (16)$$

Using equation (16) with the half-light radius of Sérsic 1, we estimate a dynamical mass of $\log_{10}(M_{\text{dyn}}/M_\odot) = 9.35 \pm 0.43$, giving a stellar mass fraction of ~ 18 per cent, consistent with predictions from simulations (de Graaff, Pillepich & Rix 2024b).

4 DISCUSSION

4.1 Physical properties

The physical properties of GNWY-7379420231 can provide insights into the formation and evolution of our galaxy, allowing us to discuss this source in the wider context of galaxy and dust formation in the early Universe. From the integrated PRISM spectrum of our source, we measure a high [O \sc{III}] + Hβ rest-frame EW of 1110 ± 183 Å, placing GNWY-7379420231 within the extreme emission-line galaxy regime (e.g. Boyett et al. 2024). The [O \sc{III}] + Hβ emission is a tracer of ongoing star formation, indicating the presence of a young stellar population. This is in agreement with the inferred mass-weighted ages (22–59 Myr) from the combined spectro-photometric SED fitting, when a UV bump is included in the attenuation curve (see Table 2). We also measure the dust-corrected emission-line ratios O32 and R23, which are shown in Fig. 7. Our source falls within the red shaded region defined in Witten et al. (2025), which indicates the region in the $\log_{10}(\text{O32}) - \log_{10}(\text{R23})$ parameter space that may be populated by galaxies containing an older stellar population.

However, in galaxies with strong emission lines, the light from recent starbursts can dominate that of older stellar populations in an effect known as 'outshining' (Narayanan et al. 2024). Due to the presence of extreme emission lines in the integrated spectrum, we investigate whether an older stellar population is present through both resolved SED fitting in Voronoi bins, and the SED fitting of the GALFIT components.

Through morphological analysis we are able to separate the source into three components: the main component (Sérsic 1), which contains the bulk of the stellar mass, and a tail made up of a second Sérsic component (Sérsic 2) and a point source. The inferred mass-weighted ages from the SED fitting of these components suggests that the main component is significantly older, with $t_\star \sim 252$ Myr, compared to $t_\star \sim 56$ Myr and $t_\star \sim 3$ Myr for the components within the tail. This indicates that an older stellar population is indeed present within GNWY-7379420231, despite the extreme emission lines dominating the integrated spectrum. The best-fitting posterior spectra are shown in Fig. 5, with the UV bump feature strongest in the point source component of the tail.

The three components identified in the morphological analysis may correspond to three distinct regions within GNWY-7379420231, where Sérsic 1 corresponds to the older stellar population with the bulk of the stellar mass, the point source corresponds to the merging clump, and Sérsic 2 is the resulting tidal tail. In order to discuss the implications of the minor merger, we isolate the merging component by identifying the region of the southern Sérsic component (Sérsic 2) that does not show any overlap with the northern Sérsic component (Sérsic 1). The isolated region includes both the point source and tidal tail, and is henceforth referred to as the merging component. This process is outlined in Appendix C with the merging component shown in Fig. C4.

We show maps of the physical properties inferred from the resolved SED fitting in Fig. 6, and UV continuum slopes measured from the median BAGPIPES posterior spectra. The overlaid contours from the SW stack show the clumpy nature of the galaxy, with a main component and an extended tail-like feature. Although clumpy morphologies are common within the EoR (Chen et al. 2024), the dissimilar SFHs of each component suggest that this may be a merger system (e.g. Hsiao et al. 2023). Furthermore, this hypothesis is supported by the detection of a tail-like feature (e.g. Ren et al. 2020).

The regions with the highest [O III] + Hβ EWs (> 2500 Å) are located across the merging component, indicating that the starburst is merger-induced. The mass-weighted ages inferred by the SED fitting for this region of extreme line emission are very young ($\lesssim 20$ Myr), further supporting the idea of a recent burst of star formation. The stellar mass surface density ($\Sigma_\star$) map shows that the bulk of the stellar mass is concentrated within the main component of the source. This could suggest the presence of an older stellar population in this region where stellar mass has built up over time. Although the $\Sigma_\star$ and SFR surface density ($\Sigma_{SFR_{10}}$) overlap significantly, there is a slight offset between the well localized peaks of the $\Sigma_{SFR_{10}}$ and $\Sigma_\star$, with the peak $\Sigma_{SFR_{10}}$ slightly closer to the merging component. Through the maps of the UV slope and A_V, we can see that the dust attenuation is patchy, with some significantly dustier sightlines present. The location of these dustier sightlines suggests that there is increased dust build-up localized to the merging component, which has $A_V \sim 0.26$ mag, compared to $A_V \sim 0.19$ mag in the main component. The bump strength (B) parameter from the Salim dust curve is a measure of the additional dust attenuation at 2175 Å and peaks within the merging component, spatially aligned with the region of extreme line emission where a recent burst of star formation took place. Note that we aim to

be conservative in our resolved bump fitting by adding a prior on B centred on $B = 0$ (see Sections 3.6 and 3.7). While our photometric analysis provides an initial insight into this spatial distribution, we note that observations with the NIRSpec IFU would be valuable to explore these findings in greater detail.

There are two possible scenarios that may give rise to the visibility of the UV bump in the merging component of GNWY-7379420231. First, an older stellar population may have enriched this region over time. The total stellar mass formed > 300 Myr ago within the main Sérsic component (Sérsic 1) is $\log_{10}(M_\star/M_\odot) = 7.96^{+0.12}_{-0.21}$. It is possible that AGB stars from this epoch could have contributed to the build-up of carbonaceous dust grains, thus contributing to the presence of the UV bump feature. In this case, the merger-induced starburst would illuminate existing dust. Alternatively, the merger-induced starburst could have processed early-formed dust, breaking down larger dust grains formed in SNe into smaller carbonaceous particles responsible for the UV bump (see Section 4.4). Although some studies suggest that small dust grains are destroyed in hard radiation fields, which leads to flatter attenuation curves with weaker UV bumps (e.g. Kriek & Conroy 2013; Tazaki, Ichikawa & Kokubo 2020), recent *JWST* observations have shown that PAHs can survive even in the harsh environments near active galactic nuclei (García-Bernete et al. 2024). As such, it remains unclear whether dust destruction, or the processing of larger grains into smaller grains, is the dominant process in hard radiation fields.

We explore the ISM properties of GNWY-7379420231 with the high-resolution G395H spectrum, dominated by emission from the merging component of the galaxy, which we use to estimate the electron density. While the obtained value is high compared to estimates based on the O32 emission-line ratio (Reddy et al. 2023), and elevated compared to galaxies at lower redshift (e.g. $n_e \sim 100$ cm^{-3}; Kaasinen et al. 2017), it is in agreement with the values obtained for galaxies at a similar redshift in Isobe et al. (2023). The high electron density ($\log_{10}(n_e)$ cm^{-1} = $3.12^{+0.83}_{-0.47}$) may be connected with gas compression as a result of the merger, potentially inducing the recent burst of star formation. Finally, we estimate the dynamical mass of our galaxy, finding a stellar mass fraction of around ~ 18 per cent, suggesting a gas-dominated system. The gas supplied by the merger would be required to fuel the strong burst of star formation. However, it must be noted that dynamical masses may be underestimated or overestimated in case of a merger (Kohandel et al. 2019; de Graaff et al. 2024a).

Finally, GNWY-7379420231 is kinematically coincident with two overdensities (JADES-GN-OD-7.133, JADES-GN-OD-7.144) identified in Helton et al. (2024), which reside in a complex environment with connected filamentary structures. Furthermore, there is evidence of accelerated galaxy evolution in protocluster environments (Morishita et al. 2025), suggesting that the large-scale environment in which GNWY-7379420231 resides could influence its evolution, contributing to rapid dust formation.

4.2 Dust attenuation curves

The dust attenuation curve assumed during SED fitting can introduce systematic biases, with properties such as stellar mass, SFR, and A_V varying significantly (Kriek & Conroy 2013; Salim & Narayanan 2020). Previous studies have shown that stellar masses and SFRs may vary by up to 0.16 and 0.3 dex, respectively (Reddy et al. 2015; Narayanan et al. 2018; Tress et al. 2018; Shivaei et al. 2020), indicating that care must be taken when carrying out SED fitting. In this section, we explore the impact of four different dust attenuation curves, three of which incorporate a UV bump.

We find that the inferred metallicity ($Z_\star$) and ionization parameter ($\log_{10} U$) are consistent regardless of the dust law assumed during SED fitting, in agreement with Markov et al. (2023). While the median mass-weighted age, $t_\star$, varies from 22 to 166 Myr, the large uncertainties associated with these inferred values have large overlap, suggesting the ages are broadly consistent regardless of the assumed dust law. However, we find that the stellar mass, $\log_{10}(M_\star/M_\odot)$, does vary depending on the assumed dust law. Adopting the flat Salim dust law gives rise to a higher stellar mass ($\log_{10}(M_*/M_\odot) = 8.84^{+0.13}_{-0.15}$, compared to $\log_{10}(M_*/M_\odot) = 8.60^{+0.15}_{-0.13}$ when assuming the standard Salim dust law). This contrasts with the consistent values inferred when adopting a dust curve which exhibits a UV bump, due to the flat Salim dust law not accounting for the deficit in the rest-UV flux caused by the UV bump, thus causing the stellar mass to be overestimated. This is also seen in Fisher et al. (2025) in sources with a strong UV bump. Additional effects of not accounting for the UV bump are documented in the literature, with changes in the estimated UV continuum slopes and dust-corrected SFRs varying by up to an order of magnitude (e.g. Buat et al. 2011; Narayanan et al. 2018; Tress et al. 2018; Shivaei et al. 2020, 2022). Therefore, care should be taken when interpreting stellar population parameters derived assuming a bump-free attenuation curve in such systems.

The SFRs and V-band dust attenuation also vary, with the use of the Li parametrization resulting in higher inferred values for both quantities.

The dust attenuation curves obtained from the BAGPIPES fitting are shown in Fig. 3, along with the commonly used Calzetti, MW, and SMC curves. We find that the dust curve obtained using the Salim et al. (2018) curve is similar to the MW dust curve within 1σ errors, with a strong UV bump at 2175 Å, with a bump strength of $B = 4.08^{+1.42}_{1.08}$, and a power-law modification of $\delta = -0.11^{+0.13}_{-0.16}$. The dust curve obtained with the Li parametrization most resembles the shape of the MW curve with the presence of the UV bump, compared to other curves such as the Calzetti and SMC curves. The dust curve obtained using the flat Salim dust curve closely resembles the Calzetti curve ($\delta = 0.03^{+0.09}_{-0.13}$).

4.3 The 2175 Å UV bump

Investigating the properties of the UV bump are crucial for understanding the evolution of cosmic dust grains. We measure a central wavelength of $\lambda_{max} = 2257^{+26}_{-28}$ Å, similar to the $\lambda_{max} = 2263^{+20}_{-24}$ Å measured in Witstok et al. (2023). This is $\sim 2.9\sigma$ higher than the peak wavelength seen in the MW curve, and may be caused by dust grains with larger molecular size (Blasberger et al. 2017; Li, Yang & Li 2024; Lin et al. 2025).

We measure a bump amplitude (strength) of $A_{\lambda,max} = 0.46^{+0.06}_{-0.07}$ mag, which we plot against cosmic time in Fig. 8, along with other high-redshift detections of the UV bump (Markov et al. 2023, 2025; Witstok et al. 2023; Fisher et al. 2025), $z \sim 2$ stacks (Noll et al. 2009; Shivaei et al. 2022), and the MW, LMC, and SMC extinction curves (Fitzpatrick & Massa 1986; Gordon et al. 2003). We note that many high-redshift galaxies do not show clear evidence for a UV bump (e.g. Markov et al. 2023, 2025; Fisher et al. 2025), and are therefore not included in this comparison. While the bump amplitudes in this work and Shivaei et al. (2022) and Witstok et al. (2023) are measured in the same way, we must convert the other literature points to a consistent definition of $A_{\lambda,max}$. We first convert the MW, LMC, and SMC curves using the Fitzpatrick & Massa (1986) definition $A_{\lambda,max} = c_3/\gamma^2 E(B - V)$, where we vary $E(B - V) = A_V/R_V$ over a range 0.1 mag $< A_V < 0.5$ mag. We convert the Noll et al. (2009) values in the same way, with the
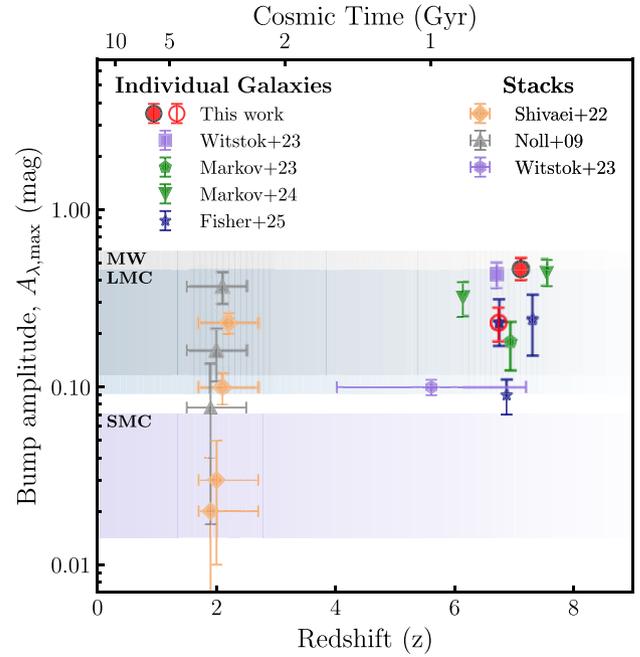
Figure 8. The bump amplitude, $A_{\lambda,max}$, as a function of redshift for individual high-redshift sources that show evidence for the presence of a UV bump (Markov et al. 2023, 2025; Witstok et al. 2023; Fisher et al. 2025), $z \sim 2$ stacks (Noll et al. 2009; Shivaei et al. 2022), and a stack of 10 $z \sim 4$–7 galaxies that show evidence for a UV bump (Witstok et al. 2023). The UV bump detected in GNWY-7379420231 is shown by the solid red circle, and the tentative UV bump detected in EGSZ-9135048459 is shown by the open red circle. The points are staggered for clarity, and the error bars along the x-axis represent the full redshift range for each stack. The shaded regions represent the average bump amplitudes in the SMC, LMC, and MW extinction curves (Fitzpatrick & Massa 1986; Gordon et al. 2003) for 0.1 mag $< A_V < 0.5$ mag.

measured values of $E(B - V)$. We convert the Markov et al. (2023) value by measuring the excess attenuation using their quoted values of c_1 to c_4 and the Li et al. (2008) dust attenuation expression as defined in their equation (6), compared to the baseline attenuation determined by setting $c_4 = 0$. Similarly, we convert the Fisher et al. (2025) values by measuring the excess attenuation using the quoted values of δ and B for the Salim dust law, and comparing to the baseline attenuation when $B = 0$. Finally, we download the spectra of the two sources identified in Markov et al. (2025) with a bump detection from the DAWN *JWST* Archive (Heintz et al. 2024), which are reduced with msaexp (Brammer 2023; de Graaff et al. 2025) to measure the bump strength and central wavelength, following the same procedure as in Section 2. We measure bump amplitudes for 2750_449 and 1433_3989 of $A_{\lambda,max} = 0.44^{+0.07}_{-0.08}$ mag and $A_{\lambda,max} = 0.32 \pm 0.07$ mag, respectively.

It is expected that the strength of the UV bump decreases towards higher redshift (Markov et al. 2025), however the bump amplitude measured in this work is high and in contrast to this expected trend. Interestingly, it is similar to the $z \sim 6.7$ detection in Witstok et al. (2023) and values we measure for the two galaxies from Markov et al. (2025). Combined with the increased peak wavelength of the bump feature in GNWY-7379420231, this suggests that the grain composition may differ compared to that at lower redshift, or these young galaxies could have a simpler dust–star geometry, as it is expected that the galaxies with the most complex young geometries have weaker bump strengths (Narayanan et al. 2018).

4.4 Dust production in the early Universe

The detection of the 2175 Å UV bump in GNWY-7379420231 provides important constraints on its dust properties and evolution. The UV bump is predominantly seen in metal-rich galaxies at $z \lesssim 3$ (e.g. Elíasdóttir et al. 2009; Noll et al. 2009; Shivaei et al. 2022), suggesting it is commonly found in evolved systems. However, recent studies have found no significant trend between gas-phase metallicity and the 2175 Å feature in local galaxies, across the metallicity range $8.40 < 12 + \log(O/H) < 8.65$ (Battisti et al. 2025).

We find that our source is metal-enriched compared to galaxies of a similar mass (Curti et al. 2024a), with $Z_{neb} \sim 0.30 Z_{\odot}$. The dust evolution within galaxies depends strongly on the age and metallicity of the system, with dust production in low-metallicity systems controlled by stellar sources (AGB stars and SNe II). When the metallicity exceeds a critical metallicity (Z_{cr}), dust mass growth becomes dominated by metal accretion on to existing dust grains within the ISM, and dust mass increases rapidly. This transition may occur at 10–20 per cent solar metallicity (e.g. Asano et al. 2013; Rémy-Ruyer et al. 2014, 2015; Li, Narayanan & Davé 2019; Roman-Duval et al. 2022). The metallicity of our system suggests that it has entered the regime of efficient ISM dust mass build-up. Additionally, Nanni et al. (2025) recently explored dust production pathways for the UV bump galaxy identified in Witstok et al. (2023), finding that when dust growth in the ISM is included, ~ 85 per cent of the carbonaceous dust production is due to dust growth.

From our SED fitting analysis of the integrated spectrum when adopting the Li dust model, we infer the presence of a very young stellar population, with $t_{\star} \sim 22$ Myr. If we were to rely solely on the stellar age inferred from the integrated spectrum in isolation, we must consider alternative dust production pathways, given that AGB stars capable of producing carbonaceous dust require a ~ 300 Myr time-scale to evolve off the main sequence.

A potential mechanism is through Wolf–Rayet (WR) stars, formed when massive stars with initial masses $> 30 M_{\odot}$ lose their hydrogen envelope. Carbon sequence WR stars (WC stars) are known to produce dust, including PAHs (Lau et al. 2022), although they may need to be in a binary system where the companion has a high mass-loss rate (e.g. Cherchneff et al. 2000; Lau et al. 2021; Peatt et al. 2023; Schneider & Maiolino 2024). However, their contribution may be limited: just 27 ± 9 per cent of WC stars display circumstellar dust within the MW (Rosslowe & Crowther 2015), and WR stars are rare (Eldridge et al. 2017), with few WC stars found in low-metallicity environments (Massey 2003). None the less, the large 0.1–1.0 µm grains produced would be more robust to destruction from the subsequent SN shocks, and have grain lifetimes approximately three times greater than 100 Å sized grains (Jones, Tielens & Hollenbach 1996). PAHs are also known to be highly stable due to their honeycomb structure (Allamandola, Tielens & Barker 1989; Tielens 2008; Lau et al. 2022).

Alternatively, early dust production could be dominated by SNe unless the reverse shock is very significant, even more so if the IMF is top-heavy (Schneider & Maiolino 2024, and references therein). Type II SNe produce dust primarily made up of silicates, amorphous carbon, magnetite, and corundum (Todini & Ferrara 2001), which can be processed into PAHs. Amorphous carbon ejected into the ISM can react with hydrogen to form hydrogenated amorphous carbons, which can then form PAHs through shattering due to grain–grain collisions (Jones et al. 1996). Additionally, photoprocessing by UV radiation can lead to the formation of aromatic bonds, with larger carbonaceous particles acting as a reservoir for the formation of smaller particles (Duley et al. 2015). Furthermore, graphitic grains

with isotopic compositions that suggest an origin in SNe have been identified, most consistent with an origin in Type II SNe (e.g. Zinner 1998; Nittler & Ciesla 2016). While the SNe reverse shock may preferentially destroy smaller grains (Nozawa et al. 2007), Jones et al. (1996) suggest that as much as 5–15 per cent of the starting graphite grain mass may end up in < 14 Å graphitic fragments, potentially forming PAHs through hydrogenation.

However, morphological analysis of our source reveals a more complex system than initially suggested by the integrated spectrum. When we examine the source as a three-component system, we find evidence for an older stellar population masked by outshining effects, a particular problem when coverage is limited to the rest-frame UV and optical (Giménez-Arteaga et al. 2024). This older stellar population is concentrated within Sérsic 1, the most massive of the three components, with a mass-weighted age of $t_{\star} = 252^{+20}_{-46}$ Myr. While stars across a broader mass range (0.8–8 $M_{\odot}$) can enter the AGB, carbon grains are mostly produced in AGB stars within the mass range $2 M_{\odot} < m_{star} < 3 - 3.5 M_{\odot}$ (Schneider & Maiolino 2024). Crucially, this component shows substantial stellar mass build-up at ages > 300 Myr, where stars $\sim 3 M_{\odot}$ enter the AGB. This could provide sufficient time for AGB driven dust production to pre-enrich the ISM before the merger event, although their evolution is less well understood in low-metallicity environments (e.g. Herwig 2005). While the SED fitting of the GALFIT components shows that the UV bump is weakest is the oldest component, this does not prevent it from playing an important role in the presence of the UV bump. Its age and stellar mass suggest a scenario in which it may have pre-enriched the surrounding ISM with carbonaceous dust grains. The contribution of this early dust build-up may now be observable, with the merger-induced starburst illuminating, or reprocessing (larger) pre-existing carbonaceous dust grains and allowing for the detection of the UV bump.

Recent galaxy evolution simulations (Narayanan et al. 2023, 2025) suggest that PAH formation is enhanced in environments with high velocity dispersions (highly turbulent gas) and strong radiation fields. Increased shattering rates are driven by these large ISM velocity dispersions in galaxies with high sSFRs, resulting in increased feedback energy per unit mass, driving up the fraction of ultrasmall grains. Furthermore, elevated global SFRs can drive aromatization by UV radiation (Narayanan et al. 2023). These theoretical predictions align with our observations of GNWY-7379420231, where the UV bump is localized to the merging component characterized by extreme [O III] + Hβ EWs and sSFRs. This spatial alignment, combined with the evidence for an older stellar population in the main component, suggests that the intense UV radiation and turbulence in the merging component may be driving localized PAH formation through both top-down shattering, as well as increased dust growth on small grains within the turbulent ISM (Narayanan et al. 2025).

5 SUMMARY

In this paper, we have presented the analysis of *JWST*/NIRSpec observations, revealing one of the most distant known galaxies exhibiting a very strong 2175 Å UV bump feature at $z = 7.11$ when the Universe was only ~ 700 Myr old. We have presented a detailed analysis of the dust properties and stellar populations within GNWY-7379420231, finding evidence for both intense ongoing star formation and an older stellar population, suggesting a complex dust production history. The spatial correlation between the UV bump and the recent burst of star formation, combined with the system likely being a merger, provides new insights into high-redshift dust evolution. Our main findings are summarized as follows:

(i) We find a strong UV bump with $A_{\lambda,\,max} = 0.46^{+0.06}_{-0.07}$ mag in a galaxy at $z = 7.11$. The peak wavelength of the UV bump is shifted by 84 Å (at 2.9σ significance) compared to that of the bump seen in the MW curve, which may suggest a different dust grain size distribution at high redshift.

(ii) While the integrated spectrum suggests a young stellar population with $t_\star \sim 22$ Myr, morphological analysis reveals the presence of an older stellar population in the most massive component with significant stellar mass with age > 300 Myr, potentially resolving the apparent tension in dust production time-scales.

(iii) Through resolved SED fitting, we determine that the UV bump is spatially correlated with the merging component, characterized by extreme [O III] + Hβ EWs, suggesting enhanced PAH formation in a turbulent environment with intense UV radiation.

(iv) We find that GNWY-7379420231 is metal-enriched compared to galaxies of a similar mass, which could indicate rapid dust mass build-up through dust grain growth mechanisms. The presence of metal enrichment could indicate that grain growth has reached an efficient growth regime, with the metal enrichment resulting from the underlying older stellar population.

In summary, we are able to provide new insights into potential dust formation and processing pathways at high redshift, suggesting that the ISM was pre-enriched by the older stellar population, before the dust was processed into PAHs through turbulence and UV radiation within the merging component. The capabilities of *JWST* will allow us to probe dust production in the early Universe in more depth, further constraining the early methods of dust production. Finding more galaxies that exhibit a UV bump, and building up a sample within the EoR will allow us to gain an understanding of the production mechanisms, the dust composition, and enable us to probe star formation and chemical evolution within the first billion years of cosmic time. Furthermore, upcoming sub-mm follow-up will provide us with multiwavelength dust constraints, such as providing an estimate of the dust-to-gas ratio of this source.

REFERENCES

Abazajian K. N. et al., 2009, ApJS, 182, 543
Abdurro'uf et al., 2024, ApJ, 973, 47
Abraham R. G., van den Bergh S., Nair P., 2003, ApJ, 588, 218
Allamandola L. J., Tielens A. G. G. M., Barker J. R., 1989, ApJS, 71, 733
Alves de Oliveira C. et al., 2018, in Peck A. B., Seaman R. L., Benn C. R., eds, Proc. SPIE Conf. Ser. Vol. 10704, Observatory Operations: Strategies, Processes, and Systems VII. SPIE, Bellingham, p. 107040Q
Asano R. S., Takeuchi T. T., Hirashita H., Inoue A. K., 2013, Earth Planets Space, 65, 213
Asplund M., Amarsi A. M., Grevesse N., 2021, A&A, 653, A141
Astropy Collaboration, 2013, A&A, 558, A33
Astropy Collaboration, 2018, AJ, 156, 123
Astropy Collaboration, 2022, ApJ, 935, 167
Austin D. et al., 2024, ApJ, preprint (arXiv:2404.10751)
Battisti A., Shivaei I., Park H. J., Decleir M., Calzetti D., Mathew J., Wisnioski E., da Cunha E., 2025, Publ. Astron. Soc. Aust., 42, e022
Blasberger A., Behar E., Perets H. B., Brosch N., Tielens A. G. G. M., 2017, ApJ, 836, 173
Böker T. et al., 2023, PASP, 135, 038001
Boucaud A., Bocchio M., Abergel A., Orieux F., Dole H., Hadj-Youcef M. A., 2016, A&A, 596, A63
Bouwens R. J. et al., 2015, ApJ, 803, 34
Boyett K. et al., 2024, MNRAS, 535, 1796
Bradley J. et al., 2005, Science, 307, 244
Brammer G., 2023, msaexp: NIRSpec analyis tools (0.6.11). Zenodo. Available at: https://doi.org/10.5281/zenodo.7939169
Brammer G. B., van Dokkum P. G., Coppi P., 2008, ApJ, 686, 1503
Buat V. et al., 2011, A&A, 533, A93
Buat V. et al., 2012, A&A, 545, A141
Buchner J. et al., 2014, A&A, 564, A125
Bunker A. J. et al., 2024, A&A, 690, A288
Calzetti D., 2013, in Falcón-Barroso J., Knapen J. H., eds, Secular Evolution of Galaxies. Cambridge Univ. Press, Cambridge, UK, p. 419

Calzetti D., Kinney A. L., Storchi-Bergmann T., 1994, ApJ, 429, 582
Calzetti D., Armus L., Bohlin R. C., Kinney A. L., Koornneef J., Storchi-Bergmann T., 2000, ApJ, 533, 682
Cameron A. J. et al., 2023, A&A, 677, A115
Caon N., Capaccioli M., D'Onofrio M., 1993, MNRAS, 265, 1013
Capak P. L. et al., 2015, Nature, 522, 455
Cappellari M., 2017, MNRAS, 466, 798
Cappellari M., 2023, MNRAS, 526, 3273
Cappellari M., Copin Y., 2003, MNRAS, 342, 345
Cardelli J. A., Clayton G. C., Mathis J. S., 1989, ApJ, 345, 245
Carnall A. C., McLure R. J., Dunlop J. S., Davé R., 2018, MNRAS, 480, 4379
Carnall A. C. et al., 2019, MNRAS, 490, 417
Carniani S. et al., 2024, A&A, 685, A99
Charlot S., Fall S. M., 2000, ApJ, 539, 718
Chen Z., Stark D. P., Mason C., Topping M. W., Whitler L., Tang M., Endsley R., Charlot S., 2024, MNRAS, 528, 7052
Cherchneff I., Le Teuff Y. H., Williams P. M., Tielens A. G. G. M., 2000, A&A, 357, 572
Chevallard J. et al., 2019, MNRAS, 483, 2621
Ciotti L., 1991, A&A, 249, 99
Ciotti L., Bertin G., 1999, A&A, 352, 447
Curti M. et al., 2024a, A&A, 684, A75
Curti M. et al., 2024b, A&A, 684, A75
Curtis-Lake E. et al., 2023, Nat. Astron., 7, 622
de Graaff A. et al., 2024a, A&A, 684, A87
de Graaff A., Pillepich A., Rix H.-W., 2024b, ApJ, 967, L40
de Graaff A. et al., 2025, A&A, 697, A189
D'Eugenio F. et al., 2024, A&A, 689, A152
Draine B., 1989, in Allamandola L. J., Tielens A. G. G. M., eds, Proc. IAU Symp. 135, Interstellar Dust. Kluwer, Dordrecht, p. 313
Duley W. W., Zaidi A., Wesolowski M. J., Kuzmin S., 2015, MNRAS, 447, 1242
Eisenstein D. J. et al., 2023, ApJS, preprint (arXiv:2306.02465)
Eldridge J. J., Stanway E. R., Xiao L., McClelland L. A. S., Taylor G., Ng M., Greis S. M. L., Bray J. C., 2017, Publ. Astron. Soc. Aust., 34, e058
Elíasdóttir Á. et al., 2009, ApJ, 697, 1725
Endsley R., Chisholm J., Stark D. P., Topping M. W., Whitler L., 2025, ApJ, 987, 189
Ferland G. J. et al., 2017, Rev. Mex. Astron. Astrofis., 53, 385
Feroz F., Hobson M. P., Bridges M., 2009, MNRAS, 398, 1601
Ferruit P. et al., 2022, A&A, 661, A81
Fisher R. et al., 2025, MNRAS, 539, 109
Fitzpatrick E. L., Massa D., 1986, ApJ, 307, 286
García-Bernete I. et al., 2024, A&A, 691, A162
Giavalisco M. et al., 2004, ApJ, 600, L93
Giménez-Arteaga C. et al., 2024, A&A, 686, A63
Gordon K. D., Clayton G. C., Misselt K. A., Landolt A. U., Wolff M. J., 2003, ApJ, 594, 279
Gordon K. D. et al., 2024, ApJ, 970, 51
Graham A. W., Driver S. P., 2005, Publ. Astron. Soc. Aust., 22, 118
Grogin N. A. et al., 2011, ApJS, 197, 35
Guthrie B. N. G., 1992, A&AS, 93, 255
Harvey T. et al., 2025, ApJ, 978, 89
Heintz K. E. et al., 2025, A&A, 693, A60
Heintz K. E. et al., 2024, Science, 384, 890
Helton J. M. et al., 2024, ApJ, 974, 41
Herwig F., 2005, ARA&A, 43, 435
Hsiao T. Y.-Y. et al., 2023, ApJ, 949, L34
Hubble E. P., 1926, ApJ, 64, 321
Isobe Y., Ouchi M., Nakajima K., Harikane Y., Ono Y., Xu Y., Zhang Y., Umeda H., 2023, ApJ, 956, 139
Jakobsen P. et al., 2022, A&A, 661, A80
Joblin C., Leger A., Martin P., 1992, ApJ, 393, L79
Jones A. P., Tielens A. G. G. M., Hollenbach D. J., 1996, ApJ, 469, 740
Kaasinen M., Bian F., Groves B., Kewley L. J., Gupta A., 2017, MNRAS, 465, 3220
Kennicutt R. C., Evans N. J., 2012, ARA&A, 50, 531

Kewley L. J., Nicholls D. C., Sutherland R. S., 2019a, ARA&A, 57, 511
Kewley L. J., Nicholls D. C., Sutherland R., Rigby J. R., Acharya A., Dopita M. A., Bayliss M. B., 2019b, ApJ, 880, 16
Koekemoer A. M. et al., 2011, ApJS, 197, 36
Kohandel M., Pallottini A., Ferrara A., Zanella A., Behrens C., Carniani S., Gallerani S., Vallini L., 2019, MNRAS, 487, 3007
Kohandel M., Pallottini A., Ferrara A., Zanella A., Rizzo F., Carniani S., 2024, A&A, 685, A72
Kriek M., Conroy C., 2013, ApJ, 775, L16
Latter W. B., 1991, ApJ, 377, 187
Lau R. M. et al., 2021, ApJ, 909, 113
Lau R. M. et al., 2022, Nat. Astron., 6, 1308
Leja J., Carnall A. C., Johnson B. D., Conroy C., Speagle J. S., 2019, ApJ, 876, 3
Leslie S. K. et al., 2018, A&A, 615, A7
Li A., Draine B. T., 2001, ApJ, 554, 778
Li A., Liang S. L., Kann D. A., Wei D. M., Klose S., Wang Y. J., 2008, ApJ, 685, 1046
Li Q., Narayanan D., Davé R., 2019, MNRAS, 490, 1425
Li Q., Yang X. J., Li A., 2024, MNRAS, 535, L58
Li S. et al., 2025, ApJ, 979, L13
Lin Q., Yang X., Li A., Witstok J., 2025, A&A, 694, A84
Looser T. J. et al., 2025, A&A, 697, A88
Lotz J. M., Primack J., Madau P., 2004, AJ, 128, 163
Lotz J. M. et al., 2008, ApJ, 672, 177
Luridiana V., Morisset C., Shaw R. A., 2015, A&A, 573, A42
Makiya R., Hirashita H., 2022, MNRAS, 517, 2076
Markov V., Gallerani S., Pallottini A., Sommovigo L., Carniani S., Ferrara A., Parlanti E., Di Mascia F., 2023, A&A, 679, A12
Markov V., Gallerani S., Ferrara A., Pallottini A., Parlanti E., Mascia F. D., Sommovigo L., Kohandel M., 2025, Nat. Astron., 9, 458
Maseda M. V. et al., 2024, A&A, 689, A73
Massey P., 2003, ARA&A, 41, 15
McElwain M. W. et al., 2023, PASP, 135, 058001
Meurer G. R., Heckman T. M., Calzetti D., 1999, ApJ, 521, 64
Morishita T. et al., 2025, ApJ, 982, 153
Nanni A., Romano M., Donevski D., Witstok J., Shivaei I., Fioc M., Sawant P., 2025, ApJL, 988, L5
Narayanan D., Conroy C., Davé R., Johnson B. D., Popping G., 2018, ApJ, 869, 70
Narayanan D. et al., 2023, ApJ, 951, 100
Narayanan D. et al., 2025, ApJ, 982, 7
Narayanan D. et al., 2024, ApJ, 961, 73
Nittler L. R., Ciesla F., 2016, ARA&A, 54, 53
Noll S., Pierini D., Pannella M., Savaglio S., 2007, A&A, 472, 455
Noll S. et al., 2009, A&A, 499, 69
Nozawa T., Kozasa T., Habe A., Dwek E., Umeda H., Tominaga N., Maeda K., Nomoto K., 2007, ApJ, 666, 955
Oke J. B., Gunn J. E., 1983, ApJ, 266, 713
Papoular R. J., Papoular R., 2009, MNRAS, 394, 2175
Peatt M. J., Richardson N. D., Williams P. M., Karnath N., Shenavrin V. I., Lau R. M., Moffat A. F. J., Weigelt G., 2023, ApJ, 956, 109
Peng C. Y., Ho L. C., Impey C. D., Rix H.-W., 2002, AJ, 124, 266
Peng C. Y., Ho L. C., Impey C. D., Rix H.-W., 2010, AJ, 139, 2097
Rauscher B. J. et al., 2017, PASP, 129, 105003
Reddy N. A. et al., 2015, ApJ, 806, 259
Reddy N. A. et al., 2020, ApJ, 902, 123
Reddy N. A., Topping M. W., Sanders R. L., Shapley A. E., Brammer G., 2023, ApJ, 952, 167
Rémy-Ruyer A. et al., 2014, A&A, 563, A31
Rémy-Ruyer A. et al., 2015, A&A, 582, A121
Ren J. et al., 2020, MNRAS, 499, 3399
Rieke M. J. et al., 2023, ApJS, 269, 16
Rigby J. et al., 2023, PASP, 135, 048001
Roberts-Borsani G. W. et al., 2016, ApJ, 823, 143
Roberts-Borsani G. et al., 2023, ApJ, 948, 54
Rodriguez-Gomez V. et al., 2019, MNRAS, 483, 4140
Roman-Duval J. et al., 2022, ApJ, 928, 90

Rosslowe C. K., Crowther P. A., 2015, MNRAS, 447, 2322
Salim S., Narayanan D., 2020, ARA&A, 58, 529
Salim S. et al., 2016, ApJS, 227, 2
Salim S., Boquien M., Lee J. C., 2018, ApJ, 859, 11
Sanders R. L. et al., 2024a, ApJ, preprint (arXiv:2408.05273)
Sanders R. L., Shapley A. E., Topping M. W., Reddy N. A., Brammer G. B., 2024b, ApJ, 962, 24
Sargent M. T. et al., 2010, ApJ, 714, L113
Saxena A. et al., 2024a, preprint (arXiv:2411.14532)
Saxena A. et al., 2024b, A&A, 684, A84
Schneider R., Maiolino R., 2024, A&AR, 32, 2
Sérsic J. L., 1963, Boletin de la Asociacion Argentina de Astronomia La Plata Argentina, 6, 41
Shivaei I. et al., 2020, ApJ, 899, 117
Shivaei I. et al., 2022, MNRAS, 514, 1886
Smit R. et al., 2015, ApJ, 801, 122
Stanway E. R., Eldridge J. J., 2018, MNRAS, 479, 75
Stecher T. P., 1965, ApJ, 142, 1683
Stecher T. P., Donn B., 1965, ApJ, 142, 1681
Tacchella S. et al., 2022, ApJ, 927, 170
Tazaki R., Ichikawa K., Kokubo M., 2020, ApJ, 892, 84
Tielens A. G. G. M., 2008, ARA&A, 46, 289
Todini P., Ferrara A., 2001, MNRAS, 325, 726
Topping M. W. et al., 2025, 541, 1707
Tress M. et al., 2018, MNRAS, 475, 2363
Vanni I., Salvadori S., Skúladóttir Á., Rossi M., Koutsouridou I., 2023, MNRAS, 526, 2620

Weaver J. R. et al., 2024, ApJS, 270, 7
Whitler L., Endsley R., Stark D. P., Topping M., Chen Z., Charlot S., 2023, MNRAS, 519, 157
Witstok J. et al., 2023, Nature, 621, 267
Witten C. et al., 2025, MNRAS, 537, 112
Yang H. et al., 2017a, ApJ, 844, 171
Yang H., Malhotra S., Rhoads J. E., Wang J., 2017b, ApJ, 847, 38
York D. G. et al., 2000, AJ, 120, 1579
Yuan Q.-r., Zhu C.-x., 2004, Chin. Astron. Astrophys., 28, 127
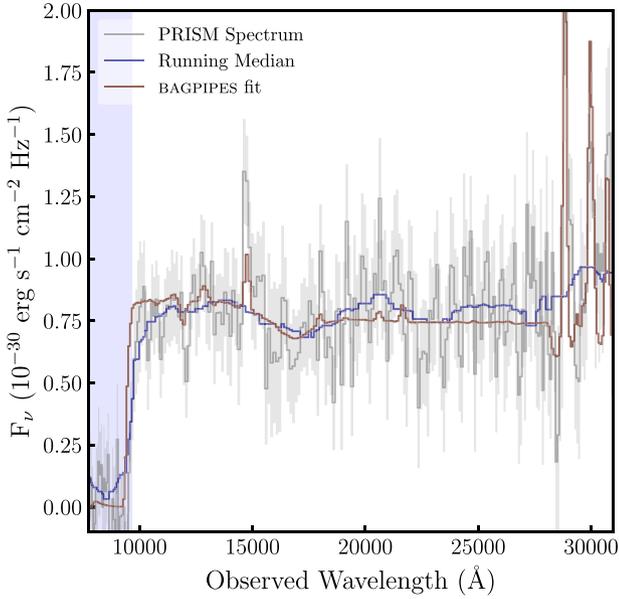Zinner E., 1998, Annu. Rev. Earth Planet. Sci., 26, 147

APPENDIX A: A TENTATIVE UV BUMP DETECTION IN EGSZ-9135048459

We detect a tentative UV bump in EGSZ-9135048459, at $z = 6.74$, shown in Fig. A1. Following the methodologies detailed in Sections 3.2 and 3.4, we fit both the UV slope and UV bump feature. We do not include EGSZ-9135048459 in the main analysis due to the tentative nature of the detection, with a 3.9σ negative flux excess. We find that the measured peak wavelength, λ_{max}, is consistent with that of the MW.

We perform SED fitting of the NIRSpec PRISM spectroscopy only, following the methodology detailed in Section 3.5. The best-fitting BAGPIPES spectrum is shown in Fig. A2, and shows tentative evidence for the presence of a UV bump.
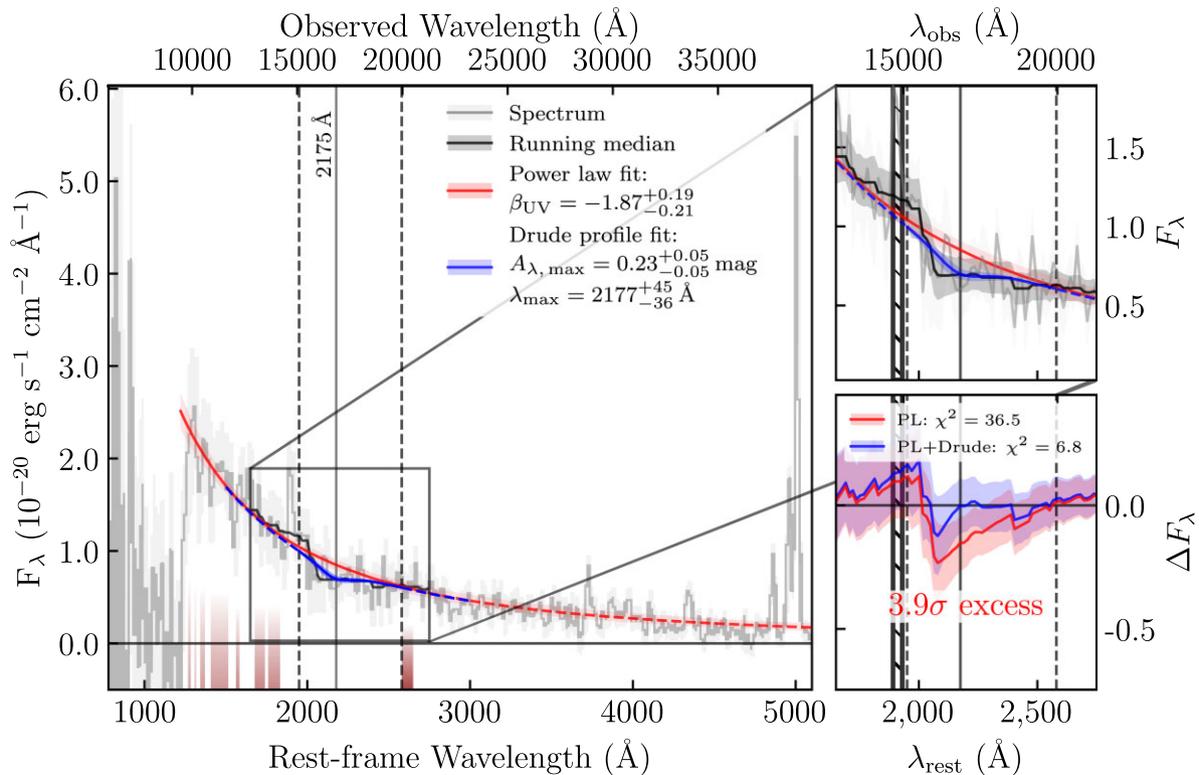
Figure A1. Spectrum of EGSZ-9135048459 (grey solid line) with a power-law fit to the UV continuum (red solid line). The dark red shading represents the UV slope fitting windows. The zoom-in panel of the region around 2175 Å shows the running median, indicated by a solid black line. This represents the attenuated stellar continuum, and shows a localized absorption feature. The Drude profile fit is shown by the solid blue line, within the fitting window indicated by the vertical dashed lines. The hatched region shows the location of the C III doublet. The bottom right panel shows the residuals of the power-law fit (PL) and the combined power-law and Drude profile fit (PL + Drude). The power-law fit alone has a 3.9σ negative flux excess.
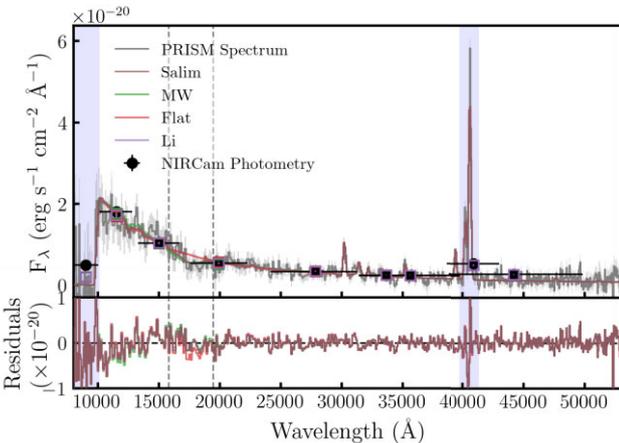
Figure A2. Posterior spectrum from BAGPIPES fitting of NIRSpec PRISM observations of EGSZ-9135048459. The observed spectrum and uncertainties are shown in grey, with the running median overlaid in dark blue. The best-fitting BAGPIPES model spectrum is displayed in dark red.

APPENDIX B: SED FITTING

The priors used for our BAGPIPES SED fitting in Section 3.5 are summarized in Table B1.

We show the BAGPIPES posterior spectra obtained in Section 3.5, with residuals, in Fig. B1.

In Fig. B2, we show the BAGPIPES posterior spectrum obtained by fitting the photometry alone, following the method in Section 3.5, with the Salim dust law.

Figure B1. Top: posterior spectra obtained from BAGPIPES fitting. The observed spectrum and associated errors are shown in grey, with the observed NIRCam photometry shown in black. The x error bars represent the filter width at 50 per cent of the maximum transmission. The posterior photometric points obtained from BAGPIPES are shown by open squares. Bottom: the residuals from the BAGPIPES fitting. The dashed vertical lines show the UV bump fitting region, and the blue shaded regions show the spectral regions masked in the BAGPIPES fitting.

Table B1. Summary of SED fitting parameters and priors used in our BAGPIPES fitting in Section 3.5. The minimum and maximum values allowed are given in brackets. The top section gives the shared parameters, which are the same regardless of the dust attenuation curve used. The following sections give model-specific parameters used with certain dust attenuation laws.

| Parameter	Prior
Shared parameters	
z	Fixed to 7.11235
$\log_{10}(M_\star/M_\odot)$	uniform: (5, 12)
$Z_\star/Z_\odot$	uniform: (0, 0.5)
$\log_{10} U$	uniform: (−3, −0.5)
A_V (mag)	Gaussian: (0, 7), $\mu = 0.15$, $\sigma = 0.15$
σ_v (km s^{-1})	logarithmic: (1, 1000)
$\Delta \log(\text{SFR})_i$	Student's-t: (−50, 50)
Salim dust law	
B	uniform: (0, 10)
δ	uniform: (−0.5, 0.2)
Flat Salim dust law	
B	Fixed to 0
δ	uniform: (−0.5, 0.2)
Li dust law	
c_1	uniform: (0, 50)
c_2	uniform: (0, 20)
c_3	uniform: (−5, 75)
c_4	uniform: (0, 10)
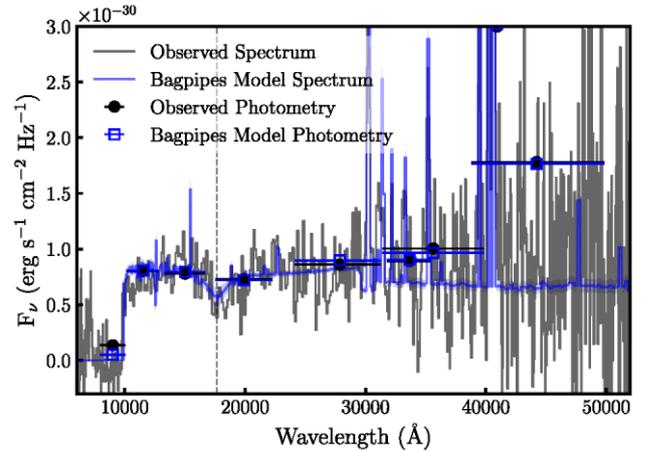
Figure B2. Posterior spectrum obtained from BAGPIPES fitting using the photometry only, shown in blue. The observed spectrum is shown in grey, with the observed NIRCam photometry shown in black. The x error bars represent the filter width at 50 per cent of the maximum transmission. The posterior photometric points obtained from BAGPIPES are shown by open blue squares. The dashed vertical line shows the location of the UV bump.

APPENDIX C: MORPHOLOGICAL FITTING

We fit each band with the best fit GALFIT model obtained in Section 3.6, leaving the magnitude free to vary. The data, model, and residual for each band is shown in Fig. C1. We also show the location of GNWY-7379420231 in the $G - M_{20}$ parameter space in Fig. C2. We show the G395H 2D spectrum of the [O III] doublet in Fig. C3.
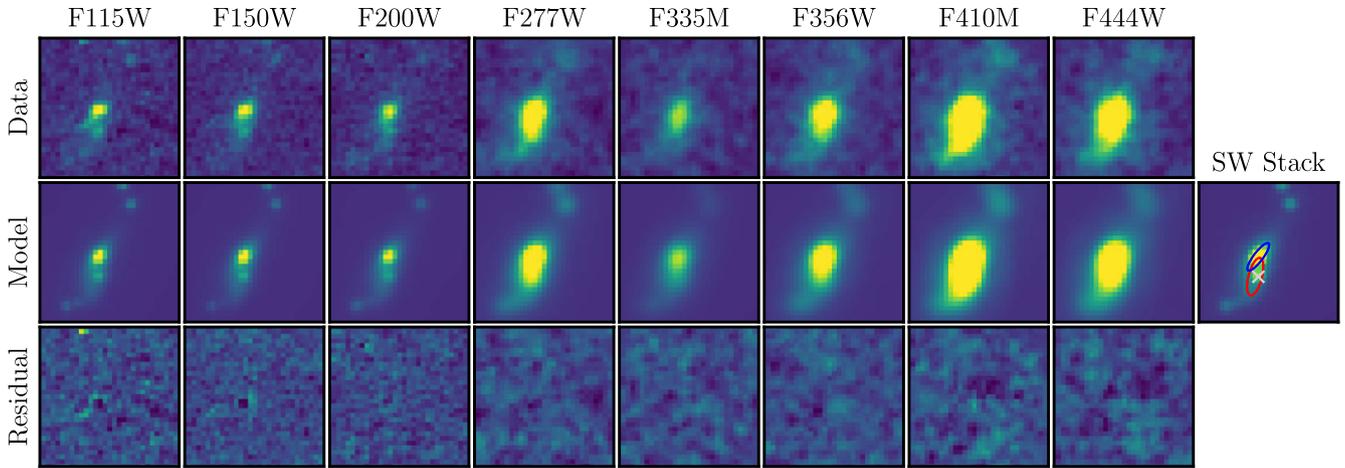
Figure C1. GALFIT fits to each band, excluding *F*090*W*. Top: the NIRCam cut-out. Middle: the GALFIT model image. Bottom: the residual image (data-model). We show the best-fitting model to the SW stack in the rightmost column for comparison, with the components overlaid. Sérsic 1 is shown in blue, Sérsic 2 in red, and the point source in the light grey cross. The data and model images in each band are linearly scaled between -3σ and 20σ of the data image background, and the residual images are scaled between -3σ and 10σ of the data image background, for clarity.
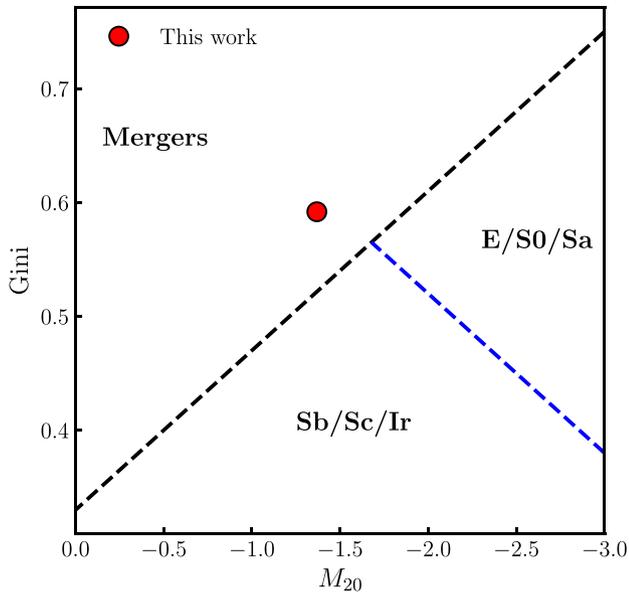

Figure C2. Gini versus M_{20} for GNWY-7379420231, measured using the SW stack. The black and blue dashed lines are from Lotz et al. (2008), and show the division between merger candidates, E/So/Sa, and Sb/Sc/Ir galaxies.

To define the region of the merging component, we first PSF match the best fit GALFIT model to the *F*444*W* image. We then define the boundary of each GALFIT component as the contour where the flux falls to 50 per cent of the component's maximum flux. The
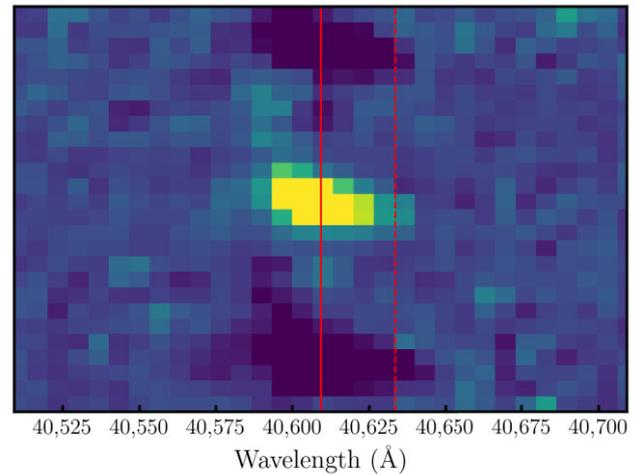
Figure C3. Zoom-in on the [O III] doublet in the G395H $R \sim 2700$ grating. The solid red line shows the location of the primary [O III] $\lambda 5007$ emission, and the red dashed line indicates the offset component, likely originating from the merging tail of the galaxy.

merging component is defined as the region of the southern Sérsic component (Sérsic 2) that does not overlap with the northern Sérsic component (Sérsic 1). The boundaries of each component and the merging component are shown in Fig. C4.
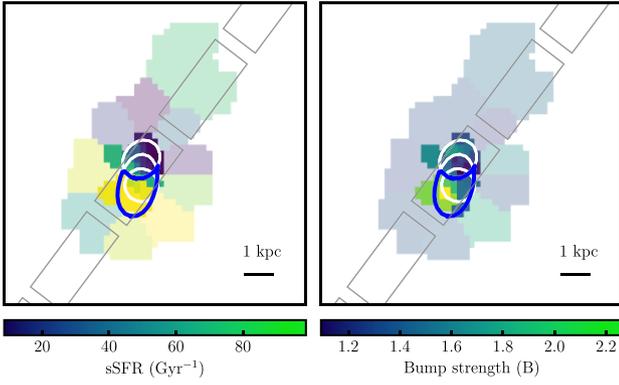
Figure C4. Maps of GNWY-7379420231, with sSFR shown in the left panel, and bump strength (B) from the Salim dust law shown in the right panel. As in Fig. 6, the fainter bins are those where the photometry has at least one band with SNR < 5 (excluding $F090W$). The borders of each component are indicated by white lines, and the border of the merging component is indicated by the blue line. The NIRSpec slitlets are overlaid in grey.

APPENDIX D: EMISSION-LINE FLUXES

Dust-corrected emission-line fluxes measured in Section 3.8 are given in Table D1. The [O II] G395H emission-line fit is shown in Fig. D1.

Table D1. Dust-corrected emission-line fluxes measured from the PRISM and G395H spectra. Fluxes are given in units of 10^{-18} erg s^{-1} cm^{-2}. [O II] $\lambda\lambda3727,29$ is blended in the PRISM spectrum, and Hβ is located within the chip-gap in the G395H spectrum.

Emission line	PRISM	G395H
[O II] $\lambda\lambda3727,29$	2.88 ± 0.53	–
[O II]$\lambda3727$	–	1.10 ± 0.28
[O II]$\lambda3729$	–	0.80 ± 0.26
Hβ	0.89 ± 0.33	–
[O III]$\lambda4959$	2.94 ± 0.11	3.61 ± 0.21
[O III]$\lambda5007$	8.76 ± 0.32	9.96 ± 0.05
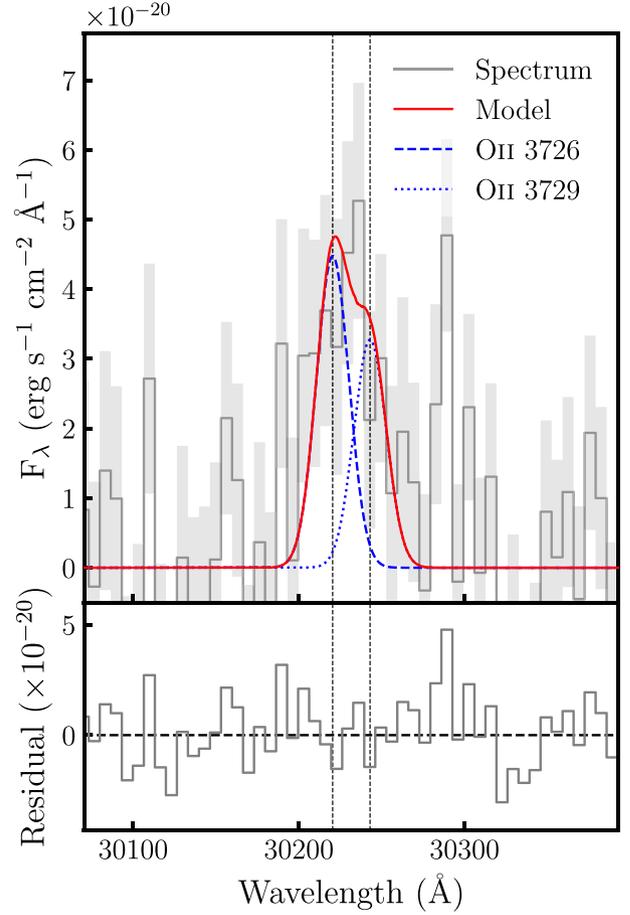
Figure D1. Double Gaussian fit to the O II high-resolution G395H spectrum (grey solid line). The red solid line represents the overall model, convolved with the G395H LSF. The blue dashed and blue dotted lines represent the intrinsic fits to the individual emission lines. The bottom panel shows the residual between the spectrum and overall model. The black dashed lines show the wavelengths of the individual emission lines, which are fixed during the fitting process.

This paper has been typeset from a TeX/LaTeX file prepared by the author.